



THE HONG KONG  
POLYTECHNIC UNIVERSITY

香港理工大學

Pao Yue-kong Library

包玉剛圖書館

---

## Copyright Undertaking

This thesis is protected by copyright, with all rights reserved.

**By reading and using the thesis, the reader understands and agrees to the following terms:**

1. The reader will abide by the rules and legal ordinances governing copyright regarding the use of the thesis.
2. The reader will use the thesis for the purpose of research or private study only and not for distribution or further reproduction or any other purpose.
3. The reader agrees to indemnify and hold the University harmless from and against any loss, damage, cost, liability or expenses arising from copyright infringement or unauthorized usage.

If you have reasons to believe that any materials in this thesis are deemed not suitable to be distributed in this form, or a copyright owner having difficulty with the material being included in our database, please contact [lbsys@polyu.edu.hk](mailto:lbsys@polyu.edu.hk) providing details. The Library will look into your claim and consider taking remedial action upon receipt of the written requests.

**The Hong Kong Polytechnic University**

**Department of Applied Physics**

**KINETIC MONTE CARLO SIMULATION OF  
STRAINED HETEROEPITAXY IN THREE  
DIMENSIONS**

**Lung Man Tat**

**A thesis submitted in partial fulfillment of the  
requirements for the Degree of Master of  
Philosophy**

**July 2005**



**Pao Yue-kong Library  
PolyU · Hong Kong**



---

THE HONG KONG POLYTECHNIC UNIVERSITY

### **Certificate of originality**

I hereby declare that this thesis is my own work and that, to the best of my knowledge and belief, it reproduces no material previously published or written nor material which has been accepted for the award of any other degree or diploma, except where due acknowledgement has been made in the text.

\_\_\_\_\_ (Signed)

\_\_\_\_\_Lung Man Tat\_\_\_\_\_ (Name of student)



# Publications

- [1] M. T. Lung, Chi-Hang Lam and Leonard M. Sander: “Island, pit and groove formation in strained heteroepitaxy”, preprint for submission to *Physical Review Letters*.
- [2] Chi-Hang Lam, M.T. Lung and Leonard M. Sander: “Fast kinetic Monte Carlo simulation of morphological evolution of strained heteroepitaxy”, in preparation for submission to *Physical Review E*.



# Abstract

Morphological evolution of strained heteroepitaxial films is studied using a kinetic Monte Carlo method in three dimensions. The film-substrate structure is modeled by a cubic lattice of balls and springs representing atoms and elastic interactions. Atomic surface diffusion is simulated using an activated hopping algorithm. The hopping barrier depends on both atomic coordination and elastic stress so that poorly coordinated or highly stressed atoms hop preferentially. The elastic stress is efficiently computed repeatedly during every stage in the surface evolution using a Green's function method and a super-particle coarsening approximation.

Applying our algorithms, films of area up to 64 by 64 atoms are studied. We have simulated annealing of initially flat films. At relatively high temperature, the film surface develops ripples, which later grow into three dimensional (3D) islands. At lower temperature, two dimensional (2D) islands and 3D pits are observed. The pits subsequently develop into grooves. Simulations of film deposition are also conducted. At low deposition rate, isolated 3D islands are observed. At higher deposition rate comparable to the corresponding surface roughening rate, morphologies similar to those from annealing are observed.



# Acknowledgments

I would like to express my gratitude to my research supervisor Dr. C. H. Lam for his guidance, supervision and support throughout my period of study.

I would also like to express my gratitude to Mr. T. L. Chan for his help with the setup and maintenance of the computer cluster.

Thanks are also given to Miss. K. Y. Cheng for her suggestions regarding the use of English of this thesis.



# Contents

<b>Publications.....</b>	<b>ii</b>
<b>Abstract.....</b>	<b>iii</b>
<b>Acknowledgments.....</b>	<b>iv</b>
<b>Contents .....</b>	<b>v</b>
<b>List of figures .....</b>	<b>vii</b>
<b>1. Introduction.....</b>	<b>1</b>
1.1 Background .....	1
1.2 Literature review .....	3
1.2.1 Experiments .....	3
1.2.2 Theories .....	4
1.2.3 Simulations.....	6
1.3 Scope of investigation .....	7
<b>2. Model and algorithms .....</b>	<b>9</b>
2.1 Ball and spring model.....	9
2.2 Atomic hopping rates .....	14
2.3 Conventional method for elastic energy calculation .....	15
2.4 Sampling of hopping events.....	17
2.4.1 Acceptance-rejection algorithm .....	17
2.5 Green's function approach for elastic energy calculation.....	19
2.5.1 Ghost atoms.....	19
2.5.2 Green's function method.....	21



2.5.3 Elastic energy calculation by the principle of virtual work .....	23
2.6 Super-particle .....	24
2.7 Elastic energy estimation table.....	28
2.7.1 Elastic energy estimation .....	28
2.7.2 Building the energy estimation table.....	29
2.7.3 Local strain estimation.....	31
2.7.4 Energy bounds calculation .....	34
<b>3. Software implementation .....</b>	<b>36</b>
<b>4. Results and discussion .....</b>	<b>37</b>
4.1 Annealing.....	37
4.2 Deposition.....	43
4.3 Pits and grooves .....	46
<b>5. Conclusions.....</b>	<b>49</b>
<b>References .....</b>	<b>50</b>



# List of figures

Figure 1.1-1: Schematic diagram of the three possible growth modes: (a) Fran-van der Merwe, (b) Volmer-Weber and (c) Stranski-Krastanov..... 2

Figure 1.2-1: The surface, elastic and total energies as a function of cluster size  $n/n^*$ .  $n^*$  is defined in equation (1.2-2). ..... 5

Figure 2.1-1: Schematic diagrams of bonds connecting a bulk atom with (a) 6 nearest neighbors; (b) 12 next nearest neighbors; (c) all 18 neighboring atoms..... 10

Figure 2.1-2: Cross-section of a small lattice for a flat film on a substrate. The horizontal solid line indicates the interface between the film and the substrate. The solid circles and the grid of dotted lines represent the atoms and the reference lattice respectively. The bonds of one of the atoms to its neighbors on the plane of the cross-section are also shown. .... 12

Figure 2.1-3: Cross-section of a film with a rough surface from a small scale calculation. The displacement vector  $\vec{u}_i$  of an atom  $i$  from its reference lattice point is shown by an arrow, which points to the center of the atom from its reference point..... 13

Figure 2.5-1: Cross-section of the extended lattice. Ghost atoms (open circle) are added on top of the real atoms (solid circle). The arrows represent external forces  $\vec{f}_j^e$  and  $\vec{f}_j^e$  acting on real and ghost atoms respectively. .... 21

Figure 2.6-1: Partitioning of a  $64 \times 64$  surface into super particles. The region colored in red at the center is the ungrouped region, which contains trivial super particles. Shells of super particles are shaded in different gray levels. .... 25



Figure 2.6-2: Plot of estimated $\Delta E_m$ using super particle against actual $\Delta E_m$ . . . . .	27
Figure 2.7-1: A local region centered at site $m$ . Numbers denote the 12 surface steps. . . . .	30
Figure 2.7-2: Surface height profile outside the local region for computing the energy estimation table. The local region is shaded in red. . . . .	31
Figure 2.7-3: Plots of the estimated strain: (a) $\epsilon_{xx}$ , (b) $\epsilon_{yy}$ , (c) $(\epsilon_{xx} + \epsilon_{yy})/2$ , (d) the corresponding surface height profile. . . . .	33
Figure 2.7-4: Plot of elastic energy bounds against the actual $\Delta E_m$ . . . . .	35
Figure 4.1-1: Snapshots of annealing of film under $T=600K$ at annealing time $t=0.1$ (a), 0.15 (b), 0.2 (c) and 0.25 s (d). (e) is the 3D view of (d). . . . .	38
Figure 4.1-2: Snapshots of annealing of film under $T=1000K$ at annealing time $t=20$ (a), 50 (b), 80 (c) and 100 $\mu s$ (d). (e) is the 3D view of (d). . . . .	40
Figure 4.1-3: Plot of the surface width $w$ against annealing time $t$ for 5 independent runs from annealing of film under $T=600K$ . . . . .	41
Figure 4.1-4: Plot of the surface width $w$ against annealing time $t$ for 5 independent runs from annealing of film under $T=1000K$ . . . . .	41
Figure 4.1-5: Snapshots of annealing of film under $T=1000K$ with misfit $\epsilon=6\%$ (a), 7% (b) and 8% (c). . . . .	42
Figure 4.2-1: Surface from simulation of deposition at $T=600K$ and $10 \text{ MLs}^{-1}$ with misfit $\epsilon=8\%$ at nominal thickness of (a) 0.8ML, (b) 1.4ML and (c) 2ML thick. The substrate is indicated by the brown color in the background. . . . .	44
Figure 4.2-2: Surface from simulation of deposition at $T=1000K$ and $20000 \text{ MLs}^{-1}$ under misfit $\epsilon=8\%$ . (a) 1ML, (b) 2ML and (c) 3ML thick. . . . .	45
Figure 4.3-1: Groove formation from annealing of film under $T=600K$ with misfit $\epsilon=6\%$ . . . . .	47
Figure 4.3-2: Snapshots of annealing of film under $T=600K$ with misfit $\epsilon=6\%$ showing a	



pit turning into a groove far away from the influence of any 2D island.....48



# 1. Introduction

## 1.1 Background

Heteroepitaxy refers to crystal growth in which films and substrates are composed of different materials. The lattice constants of the two different materials are normally different and hence create an elastic strain in the film. We call this difference lattice misfit or mismatch defined as

$$\varepsilon = \frac{a_f - a_s}{a_f} \quad (1.1-1)$$

where  $a_s$  and  $a_f$  are the unstrained lattice constant of the substrate and of the film respectively.

There are three basic crystal growth modes as shown in Figure 1.1-1, namely Volmer-Weber, Frank-Van der Merwe, and Stranski-Krastanov. In Volmer-Weber growth [1], the deposited atoms constitute nuclei on the substrate which grow to form three dimensional islands. In Frank-van der Merwe growth [2], the film grows layer by layer. The Stranski-Krastanov growth [3] is an intermediate combination of the preceding two modes. In this case after forming one or more mono-layers, subsequent layer-by-layer growth becomes unfavorable and 3D islands will be formed.

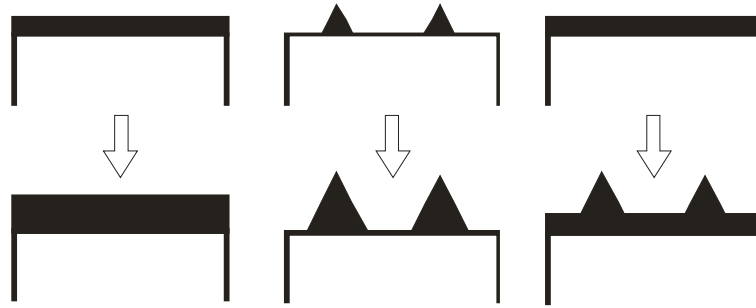


Figure 1.1-1: Schematic diagram of the three possible growth modes: (a) Fran-van der Merwe, (b) Volmer-Weber and (c) Stranski-Krastanov..

The island formation in both Volmer-Weber and Stranski-Krastanov can be coherent or incoherent. In coherent epitaxy, there is no defect at the interface. Islands form as a pathway of relaxing film stress by allowing local expansion of the lattice parameter at less constrained regions, at the cost of increasing the surface energy. In incoherent epitaxy, stress can also be relaxed by the formation of dislocations or dislocated islands.

Under appropriate conditions, coherent islands can self-assemble. They have identical shape, narrow distribution of sizes and reasonably ordered spatial distribution. These offer a promising technique for fabricating arrays of nano-sized quantum dots, which are expensive to prepare by standard lithography. These quantum nano-structures are widely expected to have potential applications in novel optoelectronic devices.

To better understand the roughening mechanism of island formation in strained layers, we have performed kinetic Monte Carlo simulations using an atomistic model. Sophisticated algorithms are adopted to achieve efficient computations. Systems with substrate containing  $64 \times 64 \times 64$  atoms were simulated.



## 1.2 Literature review

### 1.2.1 Experiments

Heteroepitaxy can be grown by molecular beam epitaxy (MBE) and similar techniques. The surface morphology of a film can be imaged using techniques such as transmission electron microscopy (TEM), atomic force microscope (AFM) and so on.

The most widely studied examples are Ge/Si and  $\text{Si}_{x-1}\text{Ge}_x/\text{Si}$  heteroepitaxy systems with misfit up to 4%. The coherent island growth process can be divided into four stages. At the early stage, the film growth layer-by-layer forming a wetting layer until a critical thickness is reached. Then ripples appear as the film continues to growth. The surface inclinations of the ripples are about  $1^\circ - 3^\circ$ . Upon further deposition, the tilt angles increase gradually to  $11.3^\circ$  characterizing (105) facets. The ripples have now turned into hut islands [4], which take the shape of a pyramid and are bounded by four (105) faceted side walls. As the film thickness continues to increase, some huts start to change its shape into domes. Dome islands [5] are more complex in shape and are composed of several types of facets including (102) and (113) surfaces. Domes exhibit a higher aspect ratio than huts, and hence relax elastic strain more effectively. This leads to the hut to dome transition.

For films of various Ge concentrations, the shapes of the islands are similar, although the size of the islands is bigger in films of lower Ge concentrations. The critical thickness for island formation is found to be a function of the Ge concentration. Both quantities are roughly proportional to  $1/x$  for  $\text{Si}_{x-1}\text{Ge}_x/\text{Si}$  films [6]. Experiments conducted by Floro *et al* [7] clearly showed the evolution of coherent Stranski-Krastanov



island growth of the  $\text{Si}_{0.8}\text{Ge}_{0.2}/\text{Si}$  system, which has a misfit about 0.8%. In their experiments, the wetting layer grew two-dimensionally up to 18 mono-layers and then ripples emerged. At 47 deposited mono-layers, the islands then developed into hut shapes. The huts can release about 20% of the stress in the film. For film thickness ranging from 94 to 150 mono-layers, huts change into domes relieving about 67% of the stress.

Pits can also form in heteroepitaxy growth. Elastic calculations [8] indicate that pits relieve more elastic energy per unit volume than islands. In general pits are observed at lower temperatures. An experiment performed by Floro *et al* [9] further shows the formation of quantum dot molecules (QDM). They grow  $\text{Si}_{0.7}\text{Ge}_{0.3}/\text{Si}$  film at  $550^\circ\text{C}$  and 0.7 ML/s. The first observed morphological feature is the formation of shallow pits with side walls at inclinations about  $2-4^\circ$ . The ejected material from the pits accumulates around the pit edges to form four islands. A pit and its four neighboring islands constitute a QDM. After further deposition, the QDMs enlarge and the walls of the central pits steepen until they facet on the (105) planes. Another experiment also performed by Gray *et al* [10] shows that pits are unstable upon annealing and elongate anisotropically into long grooves.

## 1.2.2 Theories

There are two major theories concerning about island formation in heteroepitaxy, namely the nucleation theory and the Asaro-Tiller-Grinfeld (ATG) instability theory. Nucleation theory suggests that it has to overcome an energy barrier in order to nucleate an island. The energy of an island can be expressed as [11]:

$$E = -f(\varepsilon)n + g(\gamma)n^{2/3} \quad (1.2-1)$$



The first term on the R.H.S. is the elastic energy term. The function  $f(\epsilon)$  is the elastic energy released per atom and is a function of the misfit  $\epsilon$ . The second term represents the surface energy of the island and  $g(\gamma)$  is a function of the surface energy  $\gamma$ . Figure 1.2-1 shows a sketch of the surface energy, the elastic energy and the total energy against the island size. The maximum total energy in equation (1.2-1) occurs at  $n^*$  which denotes the critical island size:

$$n^* = \left( \frac{2g(\gamma)}{3f(\epsilon)} \right)^3 \tag{1.2-2}$$

The energy barrier  $E^*$  at the critical size is

$$E^* = \frac{f(\gamma) \times n^{*2/3}}{3} \tag{1.2-3}$$

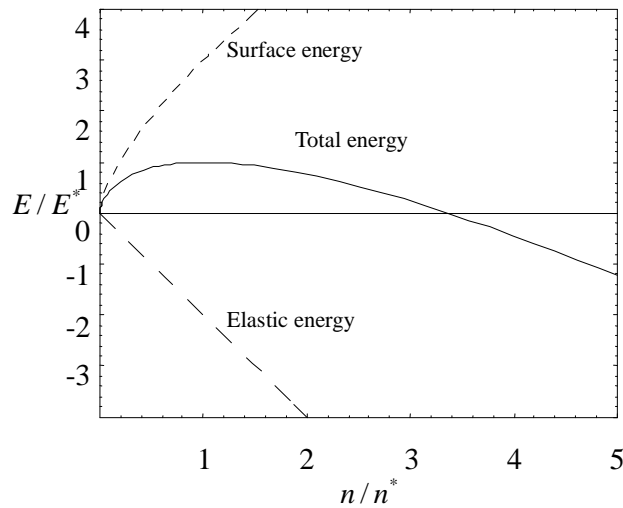


Figure 1.2-1: The surface, elastic and total energies as a function of cluster size  $n/n^*$ .  $n^*$  is defined in equation (1.2-2).



The ATG instability theory was suggested by Asaro and Tiller (1972) [12] and further investigated by Grinfeld's (1986) [13] and Srolovitz (1989) [14]. These authors studied the linear instability of a planar surface of a stressed solid. They introduce sinusoidal modulation and found that the planer surface is unstable towards perturbation at wavelengths longer than a critical value. This instability is not associated with any energy barrier and it manifests mass transport via driven surface diffusion. The stress in the solid is a destabilizing factor while the surface energy is a stabilizing one.

Considering a two-dimensional film, the shortest wavelength  $\lambda^*$  for a stable modulation can be calculated from the total energy increment per unit area due to the perturbation as a function of the amplitude  $h$  of the modulation. The surface energy increment per unit area is found to be  $E_{\text{surface}} = Ah^2 / \lambda^2$ , where  $\lambda$  is the wavelength of the sinusoidal modulation and  $A$  is a positive proportionality constant. The elastic energy increment per unit area is  $E_{\text{elastic}} = -Bh^2 \varepsilon^2 / \lambda^2$ , where  $\varepsilon$  is the lattice misfit and  $B$  is a positive constant. Then the total energy increment per unit area is  $E_{\text{total}} = E_{\text{surface}} + E_{\text{elastic}} = (A - B\varepsilon^2)h^2 \lambda^{-2}$ . For the modulation to be stable,  $E_{\text{total}}$  should be negative. Therefore, the associated wavelength should be larger than the critical value  $\lambda^* = \frac{A}{B} \varepsilon^{-2}$ .

### 1.2.3 Simulations

The first kinetic Monte Carlo (KMC) simulation of coherent island growth was conducted by Orr *et al* [15]. They used a two-dimensional solid-on-solid (SOS) ball and spring model which accounts for elastic strain. Surface diffusion is simulated by the hopping of surface atoms. The hopping probability of a surface atom depends on the



changes in the bond energy and the elastic energy upon the removal of the surface atom. They simulated in two-dimensions and used a substrate with dimensions  $75$  (width) $\times 8$  (height) atoms and rectangular islands were found. This ball and spring model is simple but can reasonably models the elastic strain. A similar version is adopted in our work.

Subsequent KMC atomistic simulations [16] report similar island formation processes. A recent two-dimensional simulation performed by Lam *et al* [17] shows ripple and then island growth using a lattice Green's function approach allowing substrate size up to  $1024\times 1024$  atoms.

### 1.3 Scope of investigation

The objective of this project is to use kinetic Monte Carlo simulation approach to study the surface roughening process in heteroepitaxy. To perform such simulation with large system size and to account for the long-range elastic interaction accurately, a huge amount of computational power is required and this is the main challenge in strained heteroepitaxy simulation. Previous simulations have used two-dimensional model to speed up the calculations. We now conduct the first three-dimensional simulations. A three-dimensional model has the advantage of the possibility of investigating both unfaceted and faceted surfaces. Moreover, islands with more realistic geometries can be studied.

We use a ball and spring model similar to those in previous works [15], but extended to three dimensions. Details will be presented in section 2.1. Elastic energy is calculated efficiently and accurately using accelerated algorithms based on the work of Lam *et al* [17], including a Green's function approach (section 2.5), a super-particle approach



(section 2.6) and an acceptance reject method (section 2.4.1) With these approaches, the computational load is reduced greatly, and systems of substrate dimensions up to  $64 \times 64 \times 64$  atoms are simulated.



## 2. Model and algorithms

This chapter will first introduce the model used in the simulation, namely the ball and spring model introduced in section 2.1. Then the surface evolution simulated by atomic surface diffusion using activated hopping will be discussed in section 2.2. The calculation of the elastic part of the activation energy will be discussed in section 2.3. Afterwards four major algorithms used in the simulation will be presented. The first one is the hopping atom sampling algorithm and will be presented in section 2.4. The second one is a Green's function approach for elastic energy calculation to be explained in section 2.5. The third one is a super-particle approach which is used to further increase the speed of the elastic energy calculation and is discussed in section 2.6. The last one is the construction and application of an elastic energy estimation table which reduces the frequency of the elastic energy calculations and will be discussed in section 2.7.

### 2.1 Ball and spring model

The film-substrate structure is modeled by balls and springs, where balls represent atoms and springs represent the bonding between atoms as shown in Figure 2.1-1. Altogether there are 18 bonds connected to each bulk atom. Six of them are connected to the nearest neighbors ( $NN$ ) and 12 of them are connected to the next nearest neighbors ( $NNN$ ).

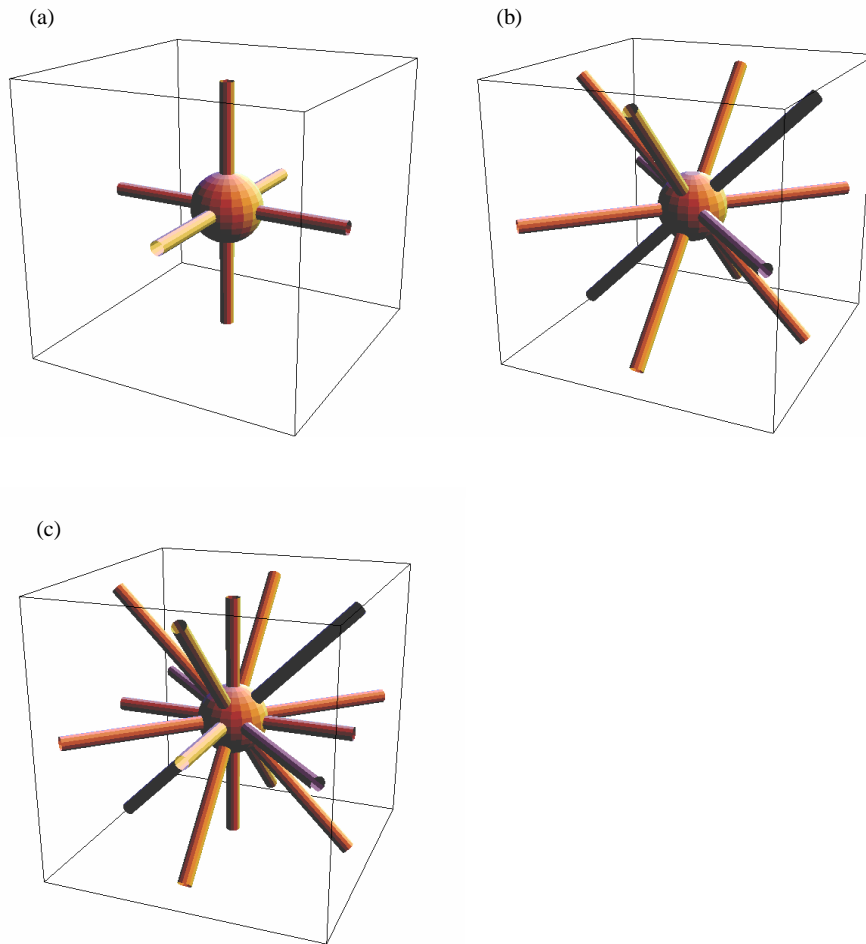


Figure 2.1-1: Schematic diagrams of bonds connecting a bulk atom with (a) 6 nearest neighbors; (b) 12 next nearest neighbors; (c) all 18 neighboring atoms.

We choose the bond strengths of  $NN$  bonds and  $NNN$  bonds to be  $\gamma_{NN} = 0.085\text{eV}$  and  $\gamma_{NNN} = \gamma_{NN}/2$  respectively. The resulting step energy in 100 and 110 directions are given by:

$$\begin{aligned}\gamma_{100} &= \gamma_{NN} + 2\gamma_{NNN} \\ \gamma_{110} &= \sqrt{2}\gamma_{NN} + \sqrt{2}\gamma_{NNN}\end{aligned}\tag{2.1-1}$$

and are equal to  $2\gamma_N$  and  $(3/2)\sqrt{2}\gamma_N$  respectively. The 2 values only differed by 6%.



The springs define the elastic properties of the materials. The elastic spring constants for  $NN$  bonds and  $NNN$  bonds are  $k_{NN} = 2eV/a_s^2$  and  $k_{NNN} = k_{NN}$  respectively. The shear moduli in 100 and 110 orientations are given by:

$$\begin{aligned} G_{100} &= k_{NNN} / a_s \\ G_{110} &= (k_{NN} + k_{NNN}) / 2a_s \end{aligned} \quad (2.1-2)$$

respectively and they are then identical. These choices of bond strengths and spring constants give reasonable isotropy of the system. We assume that the bond strength and elastic constant among pairs of atoms of types Si-Si, Ge-Ge and Si-Ge are the same. We assume a substrate lattice constant  $a_s = 2.7155 \text{ \AA}$  so that  $a_s^3$  gives the correct atomic volume in crystalline silicon. The lattice misfit is modeled by the difference between the natural length of the springs in the film and those in the substrate. A larger lattice constant  $a_f = a_s / (1 - \epsilon)$  in the film results in a compressive strain in the film. As the substrate is much thicker than the film, atoms far away from the interface in the substrate are only influenced very weakly by the film. So we assume that the atoms at the bottom layer in our lattice are fixed and held in their unstrained positions with separations equal to the lattice constant of the substrate.

We choose the atomic positions in a perfectly flat homogeneously strained film as a convenient reference lattice. The film and the substrate are arranged in rectangular and cubic lattices respectively. Solid on solid (SOS) model [18] with periodic boundary condition is assumed. The aspect ratio of the film lattice can be found easily by solving the equilibrium position of the film atoms. Figure 2.1-2 shows portion of the cross-section of the film-substrate structure near the interface. The reference lattice is indicated by the dotted lines. All atoms are positioned on the reference lattice point as the film is perfectly flat.



Some assumptions are applied in our model for better computational efficiency. The elastic couplings of adatoms with the rest of the system are weak and hence completely neglected. The heights of surface steps are limited to  $\pm 1$  atom tall. This limitation is implemented by defining the energy of the system to be positive infinity if the height of any surface step is greater than 1 atom.

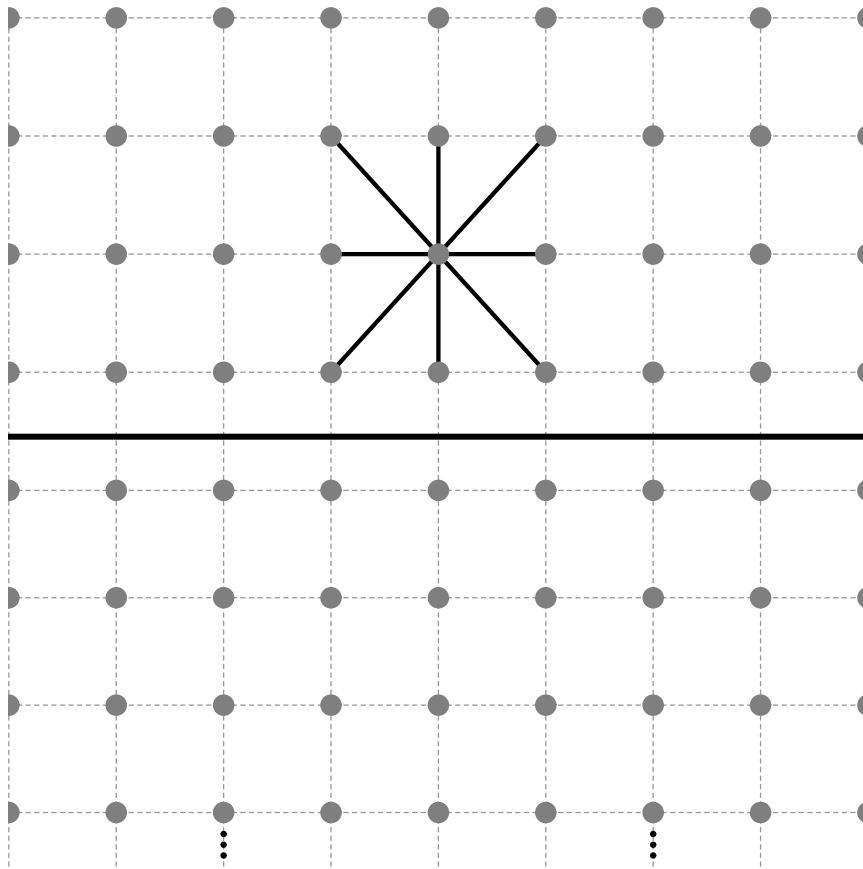


Figure 2.1-2: Cross-section of a small lattice for a flat film on a substrate. The horizontal solid line indicates the interface between the film and the substrate. The solid circles and the grid of dotted lines represent the atoms and the reference lattice respectively. The bonds of one of the atoms to its neighbors on the plane of the cross-section are also shown.



In case of a rough surface, the atoms both in the film and the substrate are no longer located at the reference lattice positions. These atoms will displace a little in order to minimize the energy. We define a displacement  $\vec{u}_i$  for each atom  $i$  measured from its reference lattice point. This notation helps reducing the complexity of the equations. Figure 2.1-3 shows the cross-section of a film with a rough surface from a small scale calculation where the displacements are indicated by arrows. We will formulate in the next section the equations needed to calculate the elastic energy.

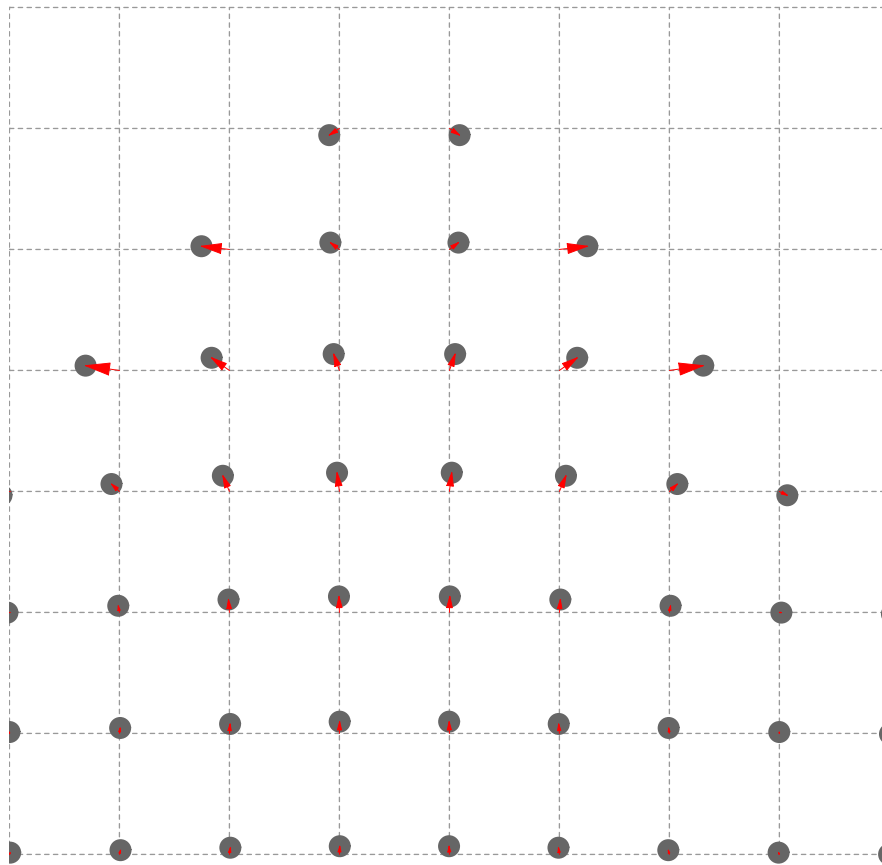


Figure 2.1-3: Cross-section of a film with a rough surface from a small scale calculation. The displacement vector  $\vec{u}_i$  of an atom  $i$  from its reference lattice point is shown by an arrow, which points to the center of the atom from its reference point.



## 2.2 Atomic hopping rates

Surface diffusion is simulated by hoppings of the topmost atoms on the film. Every topmost atom can randomly hop to a nearby topmost site within a square region of size  $(2s+1)^2$  with equal probability. The value of  $s$  used in the simulation ranges from 2 to 16. A larger value can boost the simulation speed but in case of simulating deposition with high deposition rate, a small value of  $s$  is essential in order to give correct results.

The hopping rate  $\Gamma_m$  of a topmost atom  $m$  follows the Arrhenius form:

$$\Gamma_m = R_0 \cdot \exp\left(-\frac{n_{m,NN}\gamma_{NN} + n_{m,NNN}\gamma_{NNN} + \Delta E_m + E_0}{k_B T}\right) \quad (2.2-1)$$

where  $k_B$  and  $T$  are the Boltzmann constant and the temperature respectively. We set the rate constant  $R_0 = 2D_0 / (a_s^2 \sigma^2)$ , where  $D_0 = 4.1 \times 10^{13} \text{ \AA}^2 \text{ s}^{-1}$  and  $a_s = 2.72 \text{ \AA}$  are the diffusion coefficient and the lattice constant of silicon respectively. The variance  $\sigma^2$  of the hopping distance can be calculated using  $\sigma^2 = (2s+1)^2 / 6$ . We define  $E_0 = E_a - (\gamma_{NN} + 4\gamma_{NNN})$ , where  $E_a = 0.67 \text{ eV}$  is the adatom hopping energy barrier on flat surface. The term  $n_{m,NN}\gamma_{NN} + n_{m,NNN}\gamma_{NNN}$  is the energy needed to break the bonds around atom  $m$ , where  $n_{m,NN}$  and  $n_{m,NNN}$  are the number of the nearest and next nearest neighbors of atom  $m$  respectively. The bond strength  $\gamma_{NN}$  and  $\gamma_{NNN}$  are defined in section 2.1. The calculation of the change of elastic energy  $\Delta E_m$  requires calculating twice the elastic energy of the system  $E_s$ , with and without the atom  $m$  on the surface. The calculation of  $E_s$  will be discussed in section 2.3.

In principle, due to the long range property of the elastic interactions,  $\Delta E_m$  of every site should be updated after each successful hop. The repeated calculation of  $\Delta E_m$



is computationally very intensive and is the reason why kinetic Monte Carlo simulation of strained layers is technically a much more challenging problem than its strain-free counterpart. To make the problem tractable, we need to implement efficient relaxation algorithms for the calculation of  $\Delta E_m$  which will be presented in section 2.5, 2.6 and 2.7. An equally important task is to devise a hopping algorithm that minimizes the number of such calculations. This is our acceptance-rejection method and will be discussed in section 2.4.1.

## 2.3 Conventional method for elastic energy calculation

This section will discuss about the conventional method of calculating the elastic energy  $E_S$  of a spring network under mechanical equilibrium. A more efficient algorithm for the same problem, the Green's function approach will be introduced in section 2.5.

To calculate  $E_S$ , first we need to find the equilibrium atomic positions in the spring network and then calculate the sum of the elastic energy stored in all springs. The mechanical equilibrium condition requires

$$\sum_j \vec{f}_{ij} = 0 \quad (2.3-1)$$

for every atom  $i$ . Here  $\vec{f}_{ij}$  is the force acting on atom  $i$  by its neighboring atom  $j$ , which is given by Hook's law:

$$\vec{f}_{ij} = -k_{ij} (|\vec{r}_{ij}| - l_{ij}^0) \hat{r}_{ij} \quad (2.3-2)$$

where  $k_{ij}$  is the spring constant equivalent to either  $k_{NN}$  or  $k_{NNN}$  (section 2.1) for the nearest or next nearest neighbors respectively. The natural length of the spring between the atoms



$i$  and  $j$  is denoted by  $l_{ij}^0$ . Vector  $\vec{r}_{ij}$  points from atom  $j$  to atom  $i$  and can be expressed in terms of the displacement  $\vec{u}_i$  and  $\vec{u}_j$  defined in section 2.1 as

$$\vec{r}_{ij} = \vec{u}_i - \vec{u}_j + l_{ij} \hat{n}_{ij} \quad (2.3-3)$$

where  $\hat{n}_{ij}$  is an unit vector pointing from the reference lattice point  $j$  to the point  $i$  and  $l_{ij}$  is the lattice spacing in the reference lattice. By substituting equation (2.3-3) into (2.3-2) and after linearization, we have

$$\vec{f}_{ij} = -\mathbf{K}_{ij}(\vec{u}_i - \vec{u}_j) + \vec{b}_{ij} \quad (2.3-4)$$

where the  $3 \times 3$  matrix  $\mathbf{K}_{ij} = k_{ij} \hat{n}_{ij} \hat{n}_{ij}^t$  is the modulus tensor and  $\vec{b}_{ij} = (l_{ij}^0 - l_{ij}) \mathbf{K}_{ij} \hat{n}_{ij}$  essentially represents the homogeneous stress in flat film. The condition in equation (2.3-1) leads to a large set of equations coupling  $\vec{u}_i$  with every atom  $i$ . The solution then gives the displacement  $\vec{u}_i$  for every atom and the total elastic energy  $E_s$  stored in all the springs is given by

$$E_s = \sum_{ij} \frac{k_{ij}}{2} [(\vec{u}_i - \vec{u}_j) \cdot \hat{n}_{ij} + l_{ij}^0 - l_{ij}]^2 \quad (2.3-5)$$

where the double summation is over all directly connected neighboring atoms  $i$  and  $j$ .

For our system with a substrate lattice of size  $64 \times 64 \times 64$ , there are totally about 300,000 atoms and about  $300,000 \times 3 = 900,000$  linear equations. It takes a few minutes to solve those equations to get a single value of  $E_s$  using a 2GHz PC, while  $E_s$  is typically calculated  $10^6$  times in a typical run. So it is impractical to use this conventional method to calculate  $E_s$  in a kinetic Monte Carlo simulation. The following sections in the rest of this chapter will present our methods to improve the efficiency.



## 2.4 Sampling of hopping events

In principle, the hopping rate  $\Gamma_m$  of each topmost atom  $m$  has to be calculated after each successful hop. Then a hopping site is randomly sampled with probability  $p_m$  proportional to  $\Gamma_m$ . By making use of an elastic energy bounds to be discussed in section 2.7.4 and the acceptance-rejection algorithm in section 2.4.1, we can reduce the repeated calculations of  $\Gamma_m$  drastically. Our sampling method follows detailed balance.

### 2.4.1 Acceptance-rejection algorithm

We first assume that easily computable lower and upper bounds  $\Delta E_m^\vee$  and  $\Delta E_m^\wedge$  of the change of elastic energy  $\Delta E_m$  are available (see section 2.7.4). Replacing  $\Delta E_m$  in equation (2.2-1) with  $\Delta E_m^\wedge$  we gets an upper bound

$$\Gamma_m^\wedge = R_0 \cdot \exp\left(-\frac{n_{m,NN}\mathcal{Y}_{NN} + n_{m,NNN}\mathcal{Y}_{NNN} + \Delta E_m^\wedge + E_0}{k_B T}\right) \quad (2.4-1)$$

of the hopping rate  $\Gamma_m$ . All the variables involved in the above equation are easily available and so  $\Gamma_m^\wedge$  can be updated efficiently after every hopping event. We now sample the hopping site using  $\Gamma_m^\wedge$  as the relative probability with the help of a simple binary tree data structure [19]. However some hopping sites may be over sampled since the upper bound  $\Gamma_m^\wedge$  is used instead of the true rate  $\Gamma_m$ . Hence atom  $m$  will only hop with an event acceptance probability of

$$p_m = \frac{\Gamma_m}{\Gamma_m^\wedge} = \exp\left(-\frac{\Delta E_m^\wedge - \Delta E_m}{k_B T}\right) \quad (2.4-2)$$



Up to this point, equations (2.4-1) and (2.4-2) already save us much computational efforts. However, we can do better by making use of a lower energy bound  $\Delta E_m^\vee$  and compute a lower bound  $p_m^\vee$  of the acceptance probability  $p_m$

$$p_m^\vee = \exp\left(-\frac{\Delta E_m^\wedge - \Delta E_m^\vee}{k_B T}\right) \quad (2.4-3)$$

Using an independent uniform random deviate  $\xi \in [0,1)$ , the hopping event can be accepted right away if  $\xi < p_m^\vee$ . Otherwise, we finally need to calculate  $\Delta E_m$  in order to get  $p_m$ . The sampling can still be accepted using the same random number  $\xi$ , if  $\xi < p_m$ . Otherwise it is rejected.

Note that a tighter bound of  $\Delta E_m^\vee$  and  $\Delta E_m^\wedge$  will give us a larger  $p_m^\vee$ , which result in fewer calculations of  $\Delta E_m$ . Depending on the surface roughness, typically 1 to 2 explicit elastic energy calculations are carried out before each successful hopping event. Without the acceptance-rejection method, around 5000 elastic energy calculations would have been needed. It can be shown that the above acceptance rejection scheme finally gives the correct atomic hopping rate  $\Gamma_m$  in equation (2.2-1). The time elapsed at each hop attempt, defined as a Monte Carlo step, is

$$\Delta t = 1 / \sum_m \Gamma_m^\wedge \quad (2.4-4)$$

where the summation is over every topmost site  $m$  on the surface.



## 2.5 Green's function approach for elastic energy calculation

The conventional method to calculate the elastic energy  $E_S$  of the spring system presented in section 2.3 involves solving a huge set of linear equations. However, solving large number of equations is a CPU intensive process. We now introduce a fast algorithm for computing elastic energy, which involves explicit consideration of surface atoms only. This reduces the complexity of the problem effectively by one dimension and provides significant speed up.

### 2.5.1 Ghost atoms

This Green's function approach is a lattice analog of boundary integral methods. The idea is to remove the explicit reference to all bulk atoms under the film surface from the linear equations. This is done by representing these indirect long-range interactions using appropriate lattice Green's functions. Specifically, we extend the lattice into a flat upper boundary by filling extra atoms on top of the surface with identical elastic properties to those of the film. We call these "ghost" atoms (Figure 2.5-1). The springs connecting the real and ghost atoms are unphysical. However, we can fix this by applying an external force  $\bar{f}_j^e$  on each real surface atom  $j$  so that the net unphysical force vanishes, i.e.

$$\bar{f}_j^e + \sum_j \bar{f}_{jj'} = 0 \quad (2.5-1)$$

where the summation is over all ghost neighbors  $j'$  directly connected to atom  $j$ . Applying equation (2.3-4), we get



$$\vec{f}_j^e = \sum_j [\mathbf{K}_{jj'}(\vec{u}_j - \vec{u}_{j'}) - \vec{b}_{jj'}] \quad (2.5-2)$$

The dependence on  $\vec{u}_{j'}$  is undesirable. We therefore fix the ghost atoms on the reference lattice point such that  $\vec{u}_{j'} = 0$  for all ghost atom  $j'$ . This can be achieved by applying a further external force  $\vec{f}_{j'}^e$  satisfying

$$\sum_j \vec{f}_{jj'} + \vec{f}_{j'}^e = \sum_j \vec{b}_{j'j} \quad (2.5-3)$$

where both sums are over all real neighbors  $j$  around  $j'$ . This equation states that the total force exerted on ghost atom  $j'$  by all neighboring real atoms and  $\vec{f}_{j'}^e$ , is as if the real surface atoms were at their reference lattice point.

After the condition  $\vec{u}_{j'} = 0$  is satisfied, the external forces of equations (2.5-2) and (2.5-3) can now be expressed as

$$\vec{f}_j^e = \sum_{j'} (\mathbf{K}_{jj'} \vec{u}_j - \vec{b}_{jj'}) \quad (2.5-4)$$

$$\vec{f}_{j'}^e = -\sum_j \mathbf{K}_{jj'} \vec{u}_j \quad (2.5-5)$$

using equation (2.3-4),  $\mathbf{K}_{jj'} \equiv \mathbf{K}_{j'j}$  and  $\vec{b}_{jj'} \equiv \vec{b}_{j'j}$ . In summary, after applying  $\vec{f}_j^e$  and  $\vec{f}_{j'}^e$  to the real and ghost surface atoms respectively, the real atoms are free from any unphysical forces and positioned on their proper equilibrium locations, while all ghost atoms are located at the reference lattice point. The usefulness of the ideas in this section will become clear when we come to the next section, introducing a Green's function method.

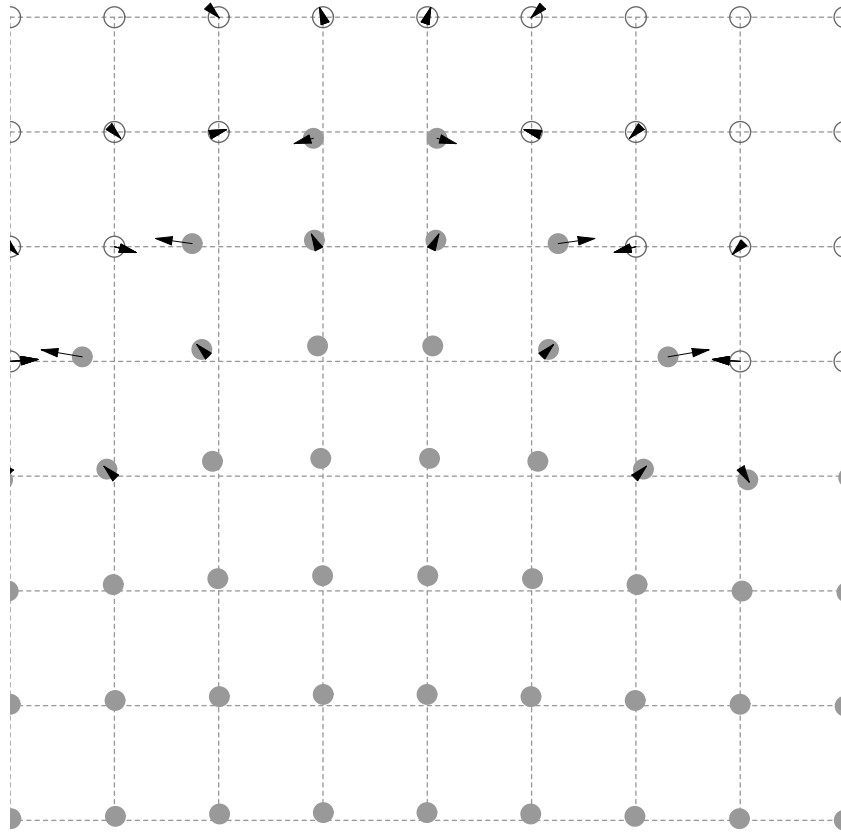


Figure 2.5-1: Cross-section of the extended lattice. Ghost atoms (open circle) are added on top of the real atoms (solid circle). The arrows represent external forces  $\vec{f}_j^e$  and  $\vec{f}_j^e$  acting on real and ghost atoms respectively.

## 2.5.2 Green's function method

We are now going to define a lattice Green's function  $\mathbf{G}_{ij}$  for the extended lattice. It is a  $3 \times 3$  matrix function of atomic positions  $i$  and  $j$  relating the displacement  $\vec{u}_i$  of atom  $i$  with an applied force  $\vec{f}_j$  on atom  $j$  by

$$\vec{u}_i = \mathbf{G}_{ij} \vec{f}_j \quad (2.5-6)$$



An important point is that  $\mathbf{G}_{ij}$  is defined for the extended lattice, which is independent of the instantaneous film morphology. Therefore it can be numerically computed before conducting the simulation using the method discussed in section 2.3, but with an additional applied force  $\bar{f}_j$ . The boundary condition is the same as the original ball and spring network described in section 2.1 except that the top layer of ghost atoms is also fixed. Note that  $\mathbf{G}_{ij}$  follows a translational symmetry in the horizontal directions and a reflection symmetry between  $x$  and  $y$  direction. It helps reducing the number of computations and the storage requirement greatly.

Applying the Green's function of equation (2.5-6) and the external forces in section (2.5.1), the displacement of any atom  $i$  is given by

$$\bar{u}_i = \sum_j \mathbf{G}_{ij} \bar{f}_j^e + \sum_{j'} \mathbf{G}_{ij'} \bar{f}_{j'}^e \quad (2.5-7)$$

Substituting the expressions for the external forces from equations (2.5-4) and (2.5-5) into this equation, we have

$$\bar{u}_i = \sum_j \sum_{j'} \mathbf{G}_{ij} (\mathbf{K}_{jj'} \bar{u}_j - \bar{b}_{jj'}) - \sum_{j'} \sum_j \mathbf{G}_{ij'} \mathbf{K}_{jj'} \bar{u}_j \quad (2.5-8)$$

It is then simplified to

$$\bar{u}_i = \sum_{jj'} [(\mathbf{G}_{ij} - \mathbf{G}_{ij'}) \mathbf{K}_{jj'} \bar{u}_j - \mathbf{G}_{ij'} \bar{b}_{jj'}] \quad (2.5-9)$$

The summation is over all real and ghost surface atoms  $j$  and  $j'$  respectively which are directly connected neighbors. With  $n_s$  real surface atoms, equation of (2.5-9) gives  $n_s$  coupled linear equations. The solution then gives the displacement  $\bar{u}_i$  of every surface atom. In principle, we can also calculate the displacement  $\bar{u}_i$  of all other atoms and hence the elastic energy  $E_s$ . In practice a more efficient method was used to calculate  $E_s$  using only the displacement of the surface atom and will be discussed in



section (2.5.3).

For our simulations with substrate dimension  $64 \times 64 \times 64$ , the number of linear equations in conventional approach discussed in section 2.3 is around 800,000. However, using the Green's function approach the number of equations reduces to roughly 10,000 and this saves a lot of CPU time and memory usage.

### 2.5.3 Elastic energy calculation by the principle of virtual work

Calculating the total elastic energy directly using equation (2.3-5) is not efficient because it requires knowing the displacement of every atom. Instead a fast algorithm is used. It needs only the displacement of the surface atoms calculated using the Green's function approach, but not those of the bulk atoms.

We now consider the original spring network without ghost atoms and external forces anymore. Then, virtual force  $\vec{f}_i^v$  is applied on every surface atom  $i$  so that the atoms are gradually pushed adiabatically back to their reference lattice positions. It's easy to see that  $\vec{f}_i^v$  is given by

$$\vec{f}_i^v = \sum_{j'} \vec{b}_{ij'} \quad (2.5-10)$$

which sums over neighboring ghost atomic position  $j'$  of atom  $i$  even though the ghost atoms are no longer present. The virtual work done by the forces is

$$W = \frac{1}{2} \sum_i [\vec{f}_i^v \cdot (-\vec{u}_i)] = -\frac{1}{2} \sum_{ij'} (\vec{b}_{ij'} \cdot \vec{u}_i) \quad (2.5-11)$$

Again, the double summation is over directly connected real and ghost pairs. Let  $E_s^{ref}$  be



the elastic energy when all the atoms are at their reference positions, and can be obtained straightforwardly from simple bond counting. Elastic energy  $E_s$  is then computed from

$$E_s = E_s^{ref} - W \quad (2.5-12)$$

Our application of equations (2.5-9) and (2.5-12) to calculate the displacement vectors  $\bar{u}_i$  and hence the elastic energy  $E_s$  respectively involves surface atoms only. Calculation of the displacement for the bulk atoms are unnecessary but can be carried out using equation (2.5-9) with the known value  $\bar{u}_j$  on the right hand side. We do this occasionally for self-consistency test.

## 2.6 Super-particle

To further improve the performance of elastic energy calculation, a super-particle approach is used. Since finding  $\Delta E_m$  require calculating  $E_s$  of the whole lattice with and without the atom at the hopping site. Obviously some surface details far away from the hopping site will not contribute much to  $\Delta E_m$  and can be neglected.

Specifically, the surface atoms are divided into groups. Each group is called a super-particle (SP). We assume that all atoms in a super-particle has identical displacement  $\bar{u}_i \equiv \bar{u}_I$  for each of its member  $i \in \Omega_I$ , where  $\Omega_I$  denotes the set of the atoms constituting super-particle  $I$ .

Our super-particles are square in shape. Their size depends on the distance with the hopping site. The super-particles are larger if it is farther away. To maximize efficiency and minimize errors, the linear size of a SP should be proportional to its distance from the hopping site. In general, all surface atoms covered by the square region of the SP are grouped together.



Surface atoms that are close enough to the hopping site (within an  $8 \times 8$  region) are also treated as a trivial SP and contain only one single atom. Outside the  $8 \times 8$  region there are square shells of super-particles. All SP within a shell are having the same size. Innermost shell ( $1^{\text{st}}$ ) have SP of size  $2 \times 2$  ( $r_1 = 2$ ), next shell have SP of size  $4 \times 4$ . In general, the size of a SP at  $n^{\text{th}}$  shell is:  $r_n = 2^n$ . The partitioning of the surface into super-particles is shown in Figure 2.6-1.

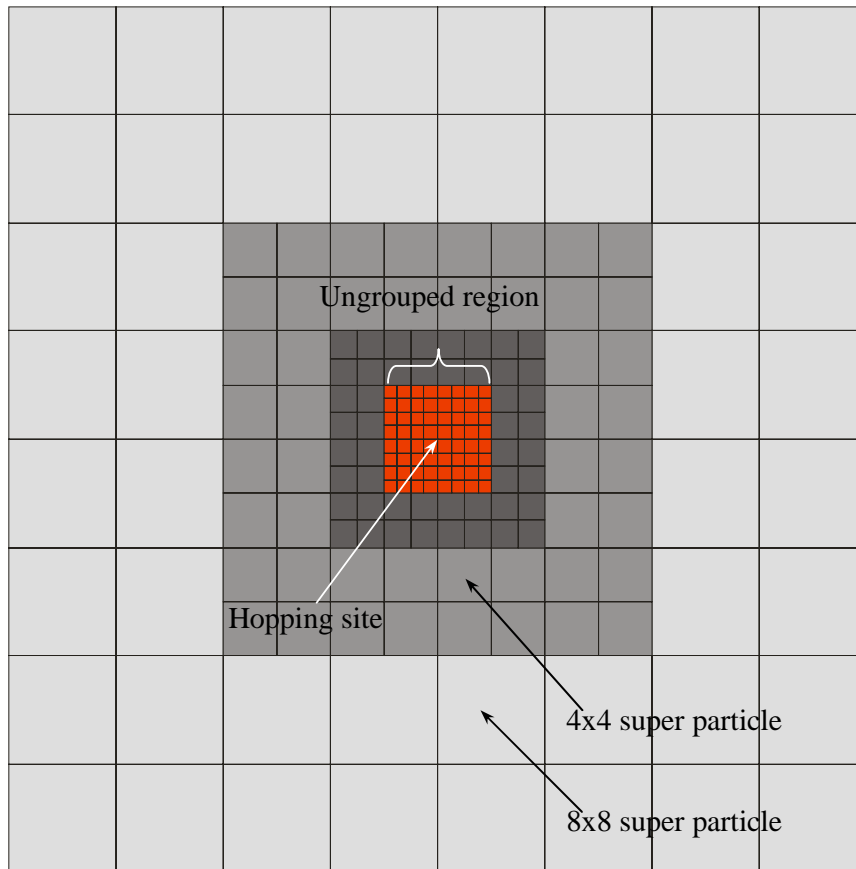


Figure 2.6-1: Partitioning of a  $64 \times 64$  surface into super particles. The region colored in red at the center is the ungrouped region, which contains trivial super particles. Shells of super particles are shaded in different gray levels.



Equation (2.5-9) is then modified into

$$\bar{u}_i = \sum_J \left\{ \left[ \sum_{j \in \Omega_j} \sum_{j'} (\mathbf{G}_{ij} - \mathbf{G}_{ij'}) \mathbf{K}_{jj'} \right] \bar{u}_j - \sum_{j \in \Omega_j} \sum_{j'} \mathbf{G}_{ij} \bar{b}_{jj'} \right\} \quad (2.6-1)$$

where  $\mathbf{G}_{ij} = \mathbf{G}_{ij}$  with the lattice point  $i$  at the centroid of the set. By solving equation (2.6-1) with bi-conjugate gradient method [20], we can get the displacement  $\bar{u}_i$  of the surface atoms and hence the elastic energy  $E_s$  of the system. Using this approach, the number of unknowns ( $\bar{u}_i$ ) can be reduced from about 5000 to about 200 for a substrate of an area of  $64 \times 64$  atoms. We expected that the number of unknowns will scale up roughly as  $\log(L)$ , where  $L \times L$  is the area of the substrate. With reduced number of unknowns, the calculation speed will become faster.

However, the operations needed to build up the coefficients of the linear equations are still enormous. As each individual constituent particle within a SP are still referenced explicitly. To facilitate further algebra, we rewrite equation (2.6-1) as

$$\bar{u}_i = \sum_J \left\{ \left[ \sum_{j \in \Omega_j} \sum_S \delta_{jS} \Delta \mathbf{G}_{ij\beta} \mathbf{K}_{j\beta} \right] \bar{u}_j - \sum_{j \in \Omega_j} \sum_S \delta_{jS} \mathbf{G}_{ij} \bar{b}_{j\beta} \right\} \quad (2.6-2)$$

where the  $S^{\text{th}}$  bond of atom  $j$  connects to atom  $\beta$ . Moreover,  $\Delta \mathbf{G}_{ij\beta} = \mathbf{G}_{ij} - \mathbf{G}_{i\beta}$  and

$$\delta_{jS} = \begin{cases} 1 & \text{if } S^{\text{th}} \text{ bond of atom } j \text{ is broken} \\ 0 & \text{otherwise} \end{cases} \quad (2.6-3)$$

Equation (2.6-2) is essentially equivalent to equation (2.6-1). Now we further approximate the summation over the individual constituent particles in equation (2.6-2) into a summation over only the 18 bond directions and write

$$\bar{u}_i = \sum_J \left\{ \left[ \sum_S n_{jS} \Delta \mathbf{G}_{ij\beta} \mathbf{K}_{j\beta} \right] \bar{u}_j - \sum_S n_{jS} \mathbf{G}_{ij} \bar{b}_{j\beta} \right\} \quad (2.6-4)$$



where  $n_{JS} = \sum_{j \in \Omega_j} \delta_{js}$  represents the number of broken bonds in SP  $J$  in the  $S^{\text{th}}$  bond direction. Now the SPs are completely characterized by their centroid positions indexed by  $I$  and  $J$ .

Equation (2.6-4) can provide a good approximation only when the SPs  $I$  and  $J$  are far apart. So we still need the more accurate equation (2.6-1) for super-particles that are close to each other when calculating the matrix coefficients. In our simulation, the error due to the super-particle approximation is typically within 5 percent as shown in Figure 2.6-2. We have also performed some numerical tests indicating that our approximation leads to no noticeable difference in our results.

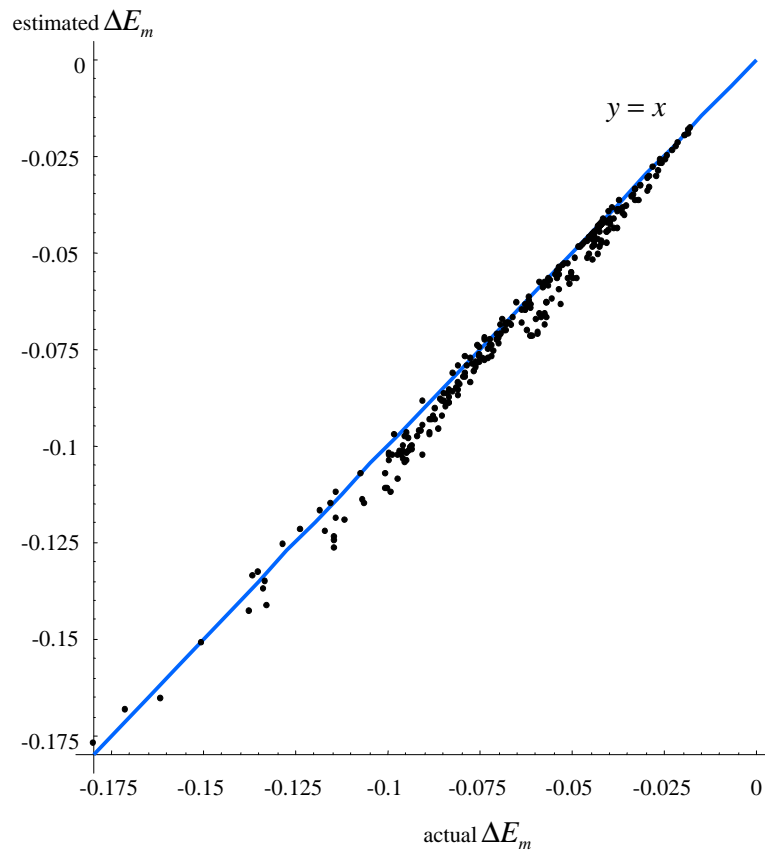


Figure 2.6-2: Plot of estimated  $\Delta E_m$  using super particle against actual  $\Delta E_m$ .



## 2.7 Elastic energy estimation table

In the acceptance-rejection algorithm presented in section 2.4.1, the lower and upper bounds  $\Delta E_m^\vee$  and  $\Delta E_m^\wedge$  respectively of the change of the elastic energy  $\Delta E_m$  at site  $m$  are needed in equations (2.4-1) and (2.4-3) during the sampling procedure (section 2.4.1). The bounds are computed by first obtaining a quick estimation of  $\Delta E_m$ , denoted by  $\Delta \tilde{E}_m$ .

### 2.7.1 Elastic energy estimation

We will first explain how to find  $\Delta \tilde{E}_m$  and the computation of the bounds will be explained later in section 2.7.4. Because  $\Delta E_m$  depends most strongly on the surface details around site  $m$ , we pre-compute  $\Delta E_m$  of all possible surface configurations within a small region around the site  $m$ , denoted by  $\Delta E_m^0$  and store their values in a table. In a 2D simulation, we can estimate  $\Delta \tilde{E}_m$  using the fact that elastic energy is proportional to the square of the strain and write

$$\Delta \tilde{E}_m = \varepsilon_{xx}^2 \frac{\Delta E_m^0}{\varepsilon_0^2} \quad (2.7-1)$$

Here  $\varepsilon_0$  is the strain used when building the table  $\Delta E_m^0$ . The choice of its value is irrelevant because  $\Delta E_m^0 \propto \varepsilon_0^2$ . The local tangential strain averaged over the local region at site  $m$  is denoted by  $\varepsilon_{xx}$ , and its calculation will be discussed later.

Equation (2.7-1) is in fact an approximation as we have neglected the shear strain  $\varepsilon_{xz}$  as well as the compressive strain  $\varepsilon_{zz}$  in the perpendicular direction. We extend



equation (2.7-1) to three dimensions by incorporating a similar average tangential strain  $\epsilon_{yy}$  in the y direction as follow

$$\Delta \tilde{E}_m = \epsilon_{xx}^2 \frac{\Delta E_x^0}{\epsilon_0^2} + \epsilon_{yy}^2 \frac{\Delta E_y^0}{\epsilon_0^2} \quad (2.7-2)$$

$\Delta E_m^0$  now consists of two terms proportional to  $\Delta E_x^0$  and  $\Delta E_y^0$ . Again, strain components other than the compressive strain  $\Delta E_m$  and  $\epsilon_{xx}$  in  $x$  and  $y$  directions are neglected. They are  $\epsilon_{zz}$ ,  $\epsilon_{xz}$ ,  $\epsilon_{yz}$  and  $\epsilon_{xy}$ . These components can be neglected because they have relatively little impact on the elastic energy  $\Delta E_m$  in our simulation. The error due to this approximation will only broaden a little the bounds  $\Delta E_m^\vee$  and  $\Delta E_m^\wedge$ , and results in a slight performance degradation on our acceptance-rejection method discussed in section 2.4.1.

## 2.7.2 Building the energy estimation table

First, we define a local region by the 12 nearest atomic columns around the hopping site  $m$  as shown in Figure 2.7-1. Note that  $\Delta E_m^0$  does not depend on the overall height of the surface, but only on the relative height within the region. For convenience, we consider site  $m$  as a reference point at 72 surface height.

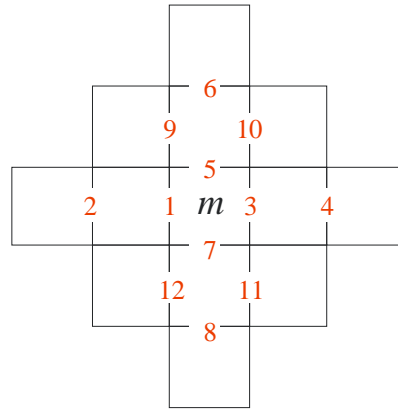


Figure 2.7-1: A local region centered at site  $m$ . Numbers denote the 12 surface steps.

We can specify the step heights at 12 surface steps in the local region in order to uniquely identify a local configuration. These step heights can be  $-1$ ,  $0$  or  $+1$ , as other values are excluded in our model. Totally, there are  $3^{12} = 531441$  possible configurations in the local region. A wider region with more configurations should give better estimation of  $\Delta\tilde{E}_m$ . However, the number of configurations is limited by the computer memory. Suppose we want to enlarge the local region by one lattice spacing step on each side, at least 8 more surface steps will be added. This will lead to  $3^{20} \approx 3.5 \times 10^9$  configurations, which is prohibitively many for our computer systems.

We use surfaces covering an area of  $32 \times 32$  atoms when building the energy estimation table. The surface configuration outside the local region is arranged as shown in Figure 2.7-2 so that the strains for various local surface configurations fluctuate around  $\varepsilon_{xx} = \varepsilon_0$  and  $\varepsilon_{yy} = 0$ . Considering the local configurations one by one with identical environment elsewhere, we calculate and store the corresponding elastic energy  $\Delta E_x^0$  using the method presented in section 2.5. The value of  $\Delta E_y^0$  also follows trivially



from the symmetry between the  $x$  and  $y$  directions. Therefore, we store  $\Delta E_x^0$  only.

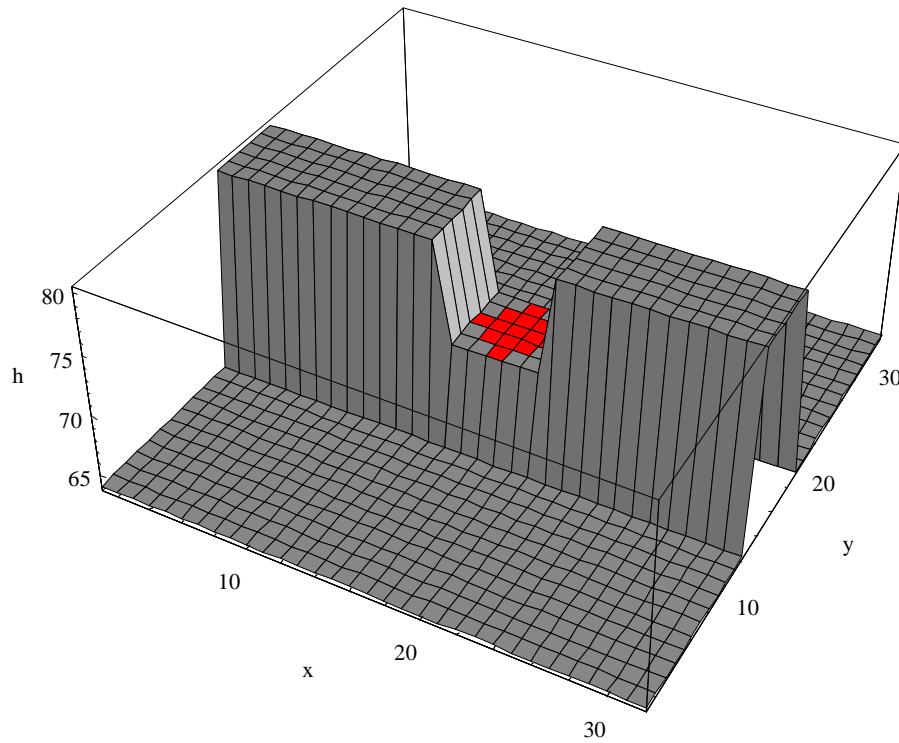


Figure 2.7-2: Surface height profile outside the local region for computing the energy estimation table. The local region is shaded in red.

### 2.7.3 Local strain estimation

In order to apply equation (2.7-2), we have to estimate the average tangential strains  $\epsilon_{xx}$  and  $\epsilon_{yy}$  in the local region due to the compression by other parts of the film. We expect  $\epsilon_{xx} \approx \epsilon$  for a relatively flat film while  $\epsilon_{xx} > \epsilon$  or  $\epsilon_{xx} < \epsilon$  for sites at a valley or a peak respectively. The same is also true for  $\epsilon_{yy}$ . Because  $\epsilon_{xx}$  and  $\epsilon_{yy}$  depend on structural



features at a longer length scale, their values change relative slowly. Therefore, we can estimate them by using also equation (2.7-2) with  $\Delta\tilde{E}_m$  replaced by the actual values of  $\Delta E_m$  from recent explicit calculations. Specifically we first define an error measure

$$\xi = (\Delta E_m - \Delta\tilde{E}_m)^2 \quad (2.7-3)$$

where  $\Delta E_m$  is the actual value from a previous explicit calculation and  $\Delta\tilde{E}_m$  is from equation (2.7-2). Differentiating the error with respect to  $\varepsilon_{xx}$  and  $\varepsilon_{yy}$  we will get

$$\frac{\partial \xi}{\partial \varepsilon_{xx}} = 4\varepsilon_{xx} \frac{\Delta E_x^0 \sqrt{\xi}}{\varepsilon_0^2} \quad (2.7-4)$$

$$\frac{\partial \xi}{\partial \varepsilon_{yy}} = 4\varepsilon_{yy} \frac{\Delta E_y^0 \sqrt{\xi}}{\varepsilon_0^2} \quad (2.7-5)$$

Then we apply the steepest descent method [21] and use equations (2.7-4) and (2.7-5) to update  $\varepsilon_{xx}$  and  $\varepsilon_{yy}$  as follows

$$\varepsilon_{xx} \leftarrow \varepsilon_{xx} - \eta \frac{\partial \xi}{\partial \varepsilon_{xx}} \quad (2.7-6)$$

$$\varepsilon_{yy} \leftarrow \varepsilon_{yy} - \eta \frac{\partial \xi}{\partial \varepsilon_{yy}} \quad (2.7-7)$$

where  $\eta$  is a rate constant. Setting  $\eta$  to 0.5 give us a reasonable performance in the simulation.

We expect that  $\varepsilon_{xx}$  and  $\varepsilon_{yy}$  change smoothly along the surface. Therefore we further use a spatial average to reduce fluctuations. After each update of  $\varepsilon_{xx}$  and  $\varepsilon_{yy}$  using equations (2.7-6) and (2.7-7), we further replace them by their spatial averages according to



$$\epsilon_{xx} \leftarrow w_1 \epsilon_{xx} + \frac{w_2}{N} \sum_i \epsilon_{i,xx} \quad (2.7-8)$$

$$\epsilon_{yy} \leftarrow w_1 \epsilon_{yy} + \frac{w_2}{N} \sum_i \epsilon_{i,yy} \quad (2.7-9)$$

Here the summation is over the 8 neighboring top-most sites around site  $m$  and  $N=8$ . We use 0.8 for  $w_1$  and 0.2 for  $w_2$ . Snapshots of the estimated strain and the corresponding surface are shown in Figure 2.7-3.

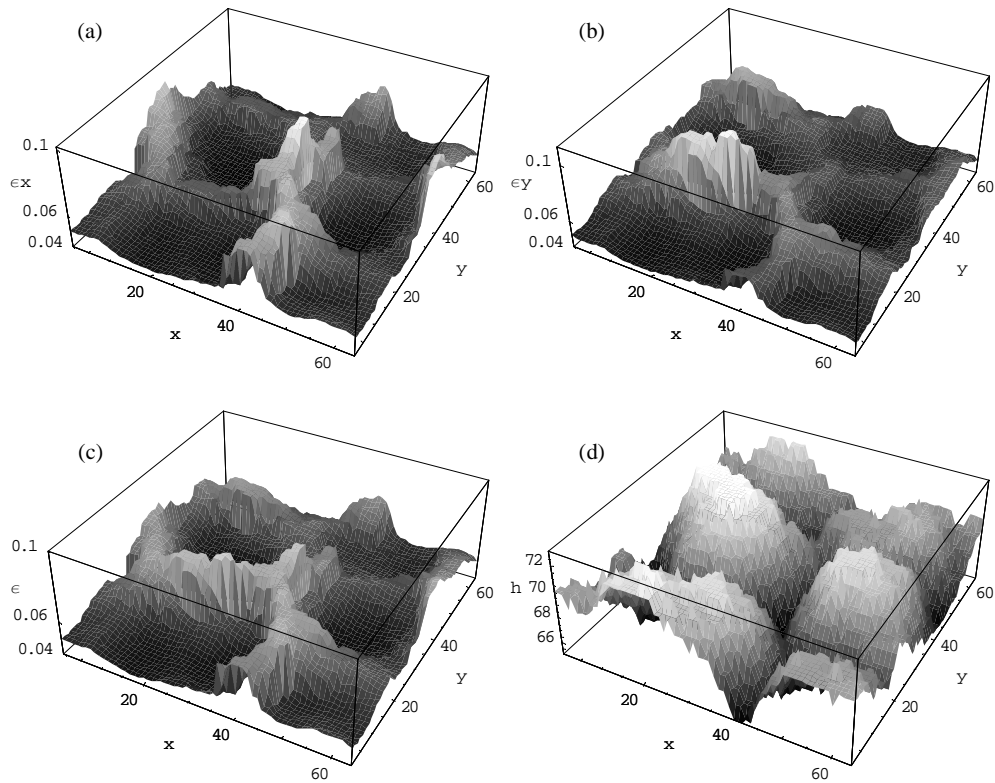


Figure 2.7-3: Plots of the estimated strain: (a)  $\epsilon_{xx}$ , (b)  $\epsilon_{yy}$ , (c)  $(\epsilon_{xx} + \epsilon_{yy})/2$ , (d) the corresponding surface height profile.



## 2.7.4 Energy bounds calculation

With an estimate  $\Delta\tilde{E}_m$  of the elastic energy as explained in section 2.7, the upper and the lower bounds are now defined by

$$\Delta E_m^\wedge = \Delta\tilde{E}_m + c^\wedge \quad (2.7-10)$$

$$\Delta E_m^\vee = \Delta\tilde{E}_m + c^\vee \quad (2.7-11)$$

where  $c^\wedge$  and  $c^\vee$  are dynamically calculated biases. Whenever an explicit calculated value of  $\Delta E_m$  is larger than the predicted upper bound  $\Delta E_m^\wedge$ ,  $c^\wedge$  will be increased to attain a more conservative bound. Otherwise it is decreased slightly for a more aggressive event acceptance rate. The algorithm for  $c^\vee$  is analogous. In our simulation,  $\Delta E_m$  actually lies outside the predicted bounds with a small frequency less than 0.5%. The resulting over and under samplings of hopping events (section 2.4.1) are expected to be negligible. Figure 2.7-4 shows a plot of the predicted bounds using equations (2.7-10) and (2.7-11).

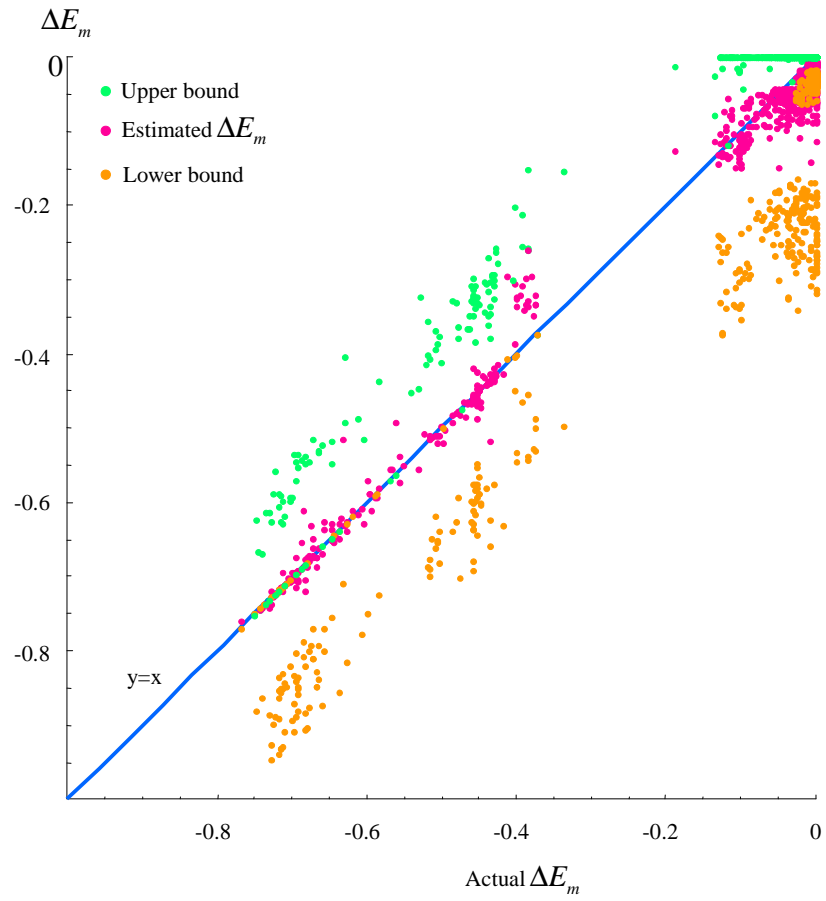


Figure 2.7-4: Plot of elastic energy bounds against the actual  $\Delta E_m$ .



## 3. Software implementation

The complexity arised from the usage of many sophisticated algorithms in this work has made the software implementation of the simulation a great challenge. The C++ language was chosen to code the simulation as it is a high level language facilitating abstracted programming while its low level language construct allows efficient run-time.

The simulation is modulated into several parts with the use of object orientated technologies. They include a core module that deal with basic input/output, database access and graphics interface etc., a class module for the hopping procedures, an energy calculation module, and a module for the elastic energy bound estimation and application. Standalone programs were also written to generate the Green's function table and the elastic energy estimation table. For the elastic energy calculation module, we have take advantages of the Intel® Math Kernel Library [22], which is highly optimized for the Intel® Pentium® architectures.

Our simulations were run under a distributed environment with up to 40 computers in a Multimedia laboratory with multiple users. Each computer was either assigned a simulation with a new set of parameters or to repeat another simulation to gain better statistics. The Cygwin [23] Linux-like environment is installed on top of the Windows® operating system, which made the job of controlling and monitoring of the simulations easier. It also allows our simulations to run in the background without disturbing other users of the computers.



## 4. Results and discussion

Annealing and deposition of heteroepitaxy systems with misfit ranged from 6% to 10% is performed. The systems we study have a higher misfit than other commonly studied cases for example the  $\text{Si}_{x-1}\text{Ge}_x/\text{Si}$  system. It is because the system size limited our island size within  $64 \times 64$ , but we expected that the results we found are also applicable to systems with lower misfit. Other model parameters used in our simulation are introduced in sections 2.1 and 2.2.

### 4.1 Annealing

We have simulated annealing of initially flat films of 10 mono-layers (ML) at temperatures  $T=600\text{K}$  and  $T=1000\text{K}$ . Figure 4.1-1 shows the surface evolution of an initially flat film of misfit  $\varepsilon=6\%$  annealed under  $T=600\text{K}$ . At this low temperature, only a limited area of the film roughens and most of the film remains flat indicating that the surface is a true facet. We believe that  $600\text{K}$  is below the roughening temperature. At the early stage of the annealing, the surface step density is low. Small 2D pits and islands emerge as shown in (a). These 2D pits and islands grow two-dimensionally and the atoms ejected from the pits accumulate as islands. We observe that pits or islands grow steadily only after the corresponding critical sizes associated with 2D nucleation barriers (section 1.2.2) were reached as shown in (c) and (d). Note that pits are more abundant than islands. Moreover, pits are three-dimensional while islands are two-dimensional. These can be explained by the fact that pits can relieve more energy per unit volume than islands [25] and hence a lower energy barrier.

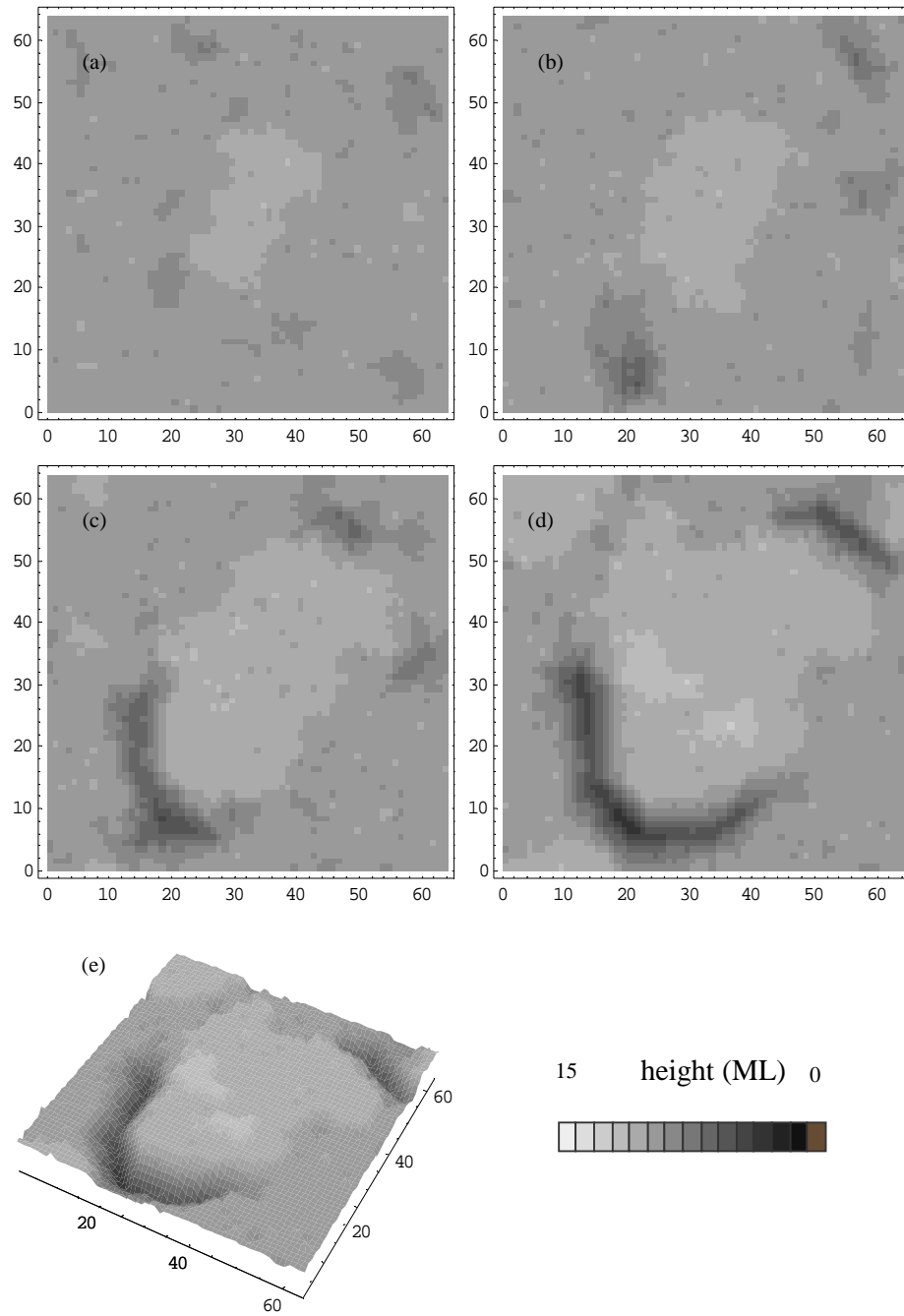


Figure 4.1-1: Snapshots of annealing of film under  $T=600K$  at annealing time  $t=0.1$  (a),  $0.15$  (b),  $0.2$  (c) and  $0.25$  s (d). (e) is the 3D view of (d).



For the case of high temperature annealing under  $T=1000K$  as shown in Figure 4.1-2, we found that the surface roughen following the ATG instability that was discussed in section 1.2.3. The abundant steps indicated that the surface is not a true facet at  $1000K$ ; therefore this temperature is beyond the surface roughening transition point. Ripple-like perturbations emerge gradually with local surface inclinations increasing steadily and relatively synchronously in agreement with experiments [7] and the ATG instability as shown in (a) to (c). Later on, the islands are well developed and are bounded by network of grooves as shown in (d). Note that the surface inclination at the grooves and to certain extend of the islands have reached its maximum value allowed in our model.

The mechanism selection between nucleation and instability is further investigated quantitatively by studying the r.m.s. surface width  $w$  against the annealing time  $t$ . Figure 4.1-3 shows a plot of the surface width against time for 5 independent runs of annealing under  $T=600K$ . There are large ensemble fluctuations among the 5 runs. This further supports the relevance of nucleation processes. Figure 4.1-4 shows a similar plot for annealing at  $T=1000K$ . In sharp contrast with the previous graph, the width increases gradually with small ensemble fluctuations which are characteristic features of barrierless processes.

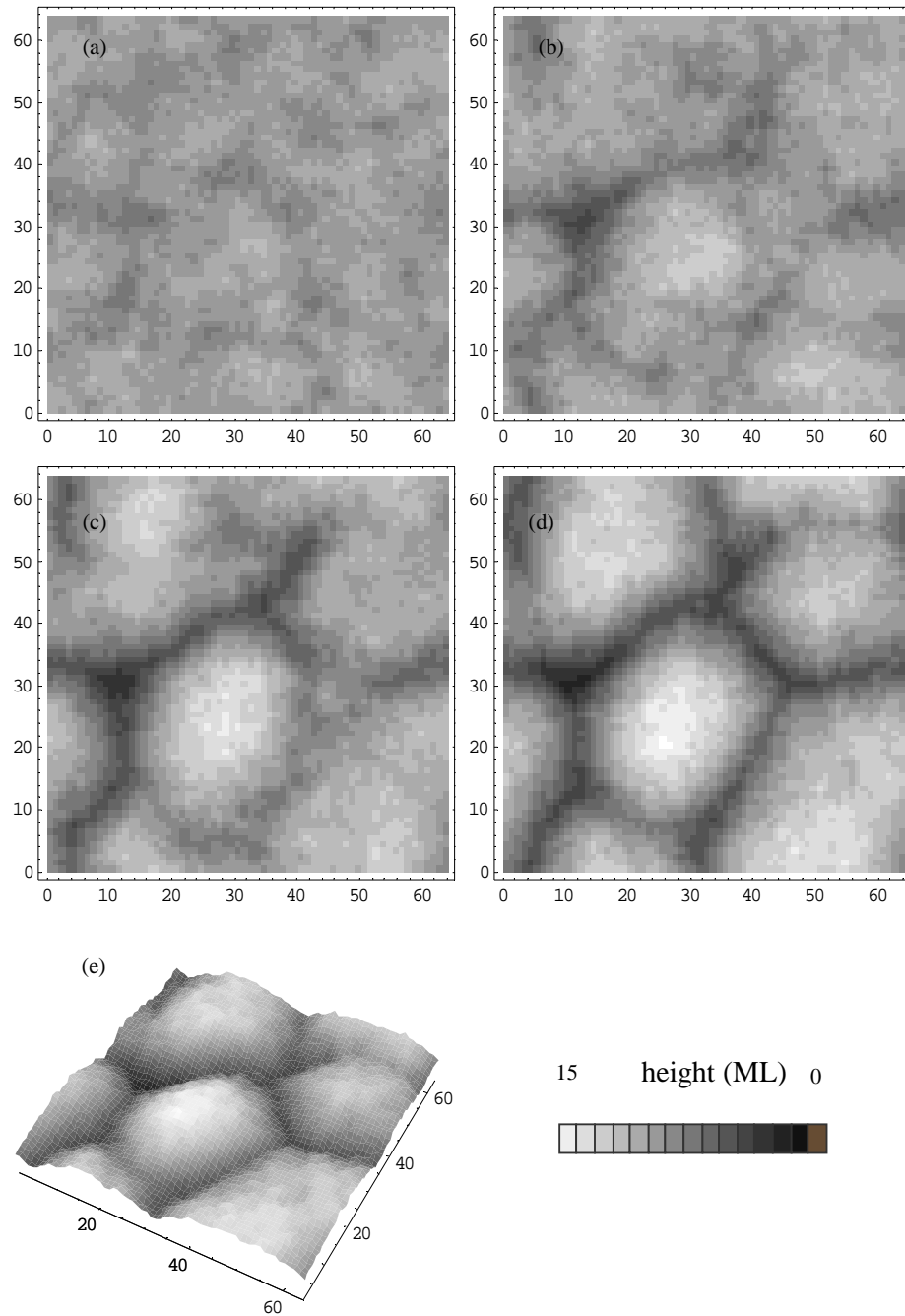


Figure 4.1-2: Snapshots of annealing of film under  $T=1000K$  at annealing time  $t=20$  (a), 50 (b), 80 (c) and  $100 \mu s$  (d). (e) is the 3D view of (d).

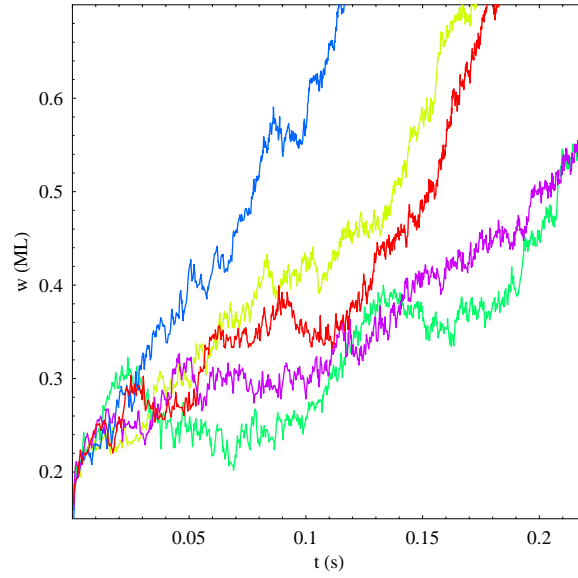


Figure 4.1-3: Plot of the surface width  $w$  against annealing time  $t$  for 5 independent runs from annealing of film under  $T=600K$ .

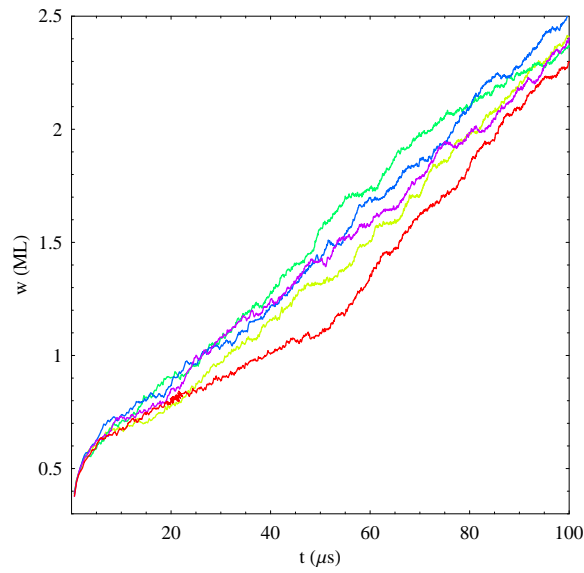


Figure 4.1-4: Plot of the surface width  $w$  against annealing time  $t$  for 5 independent runs from annealing of film under  $T=1000K$ .



Simulations of annealing with different misfit under high temperature are studied. The resulting surfaces are shown in Figure 4.1-5. The islands size decrease with increasing misfit as we expected from experiments and theories. However, a more quantitative analysis is obstructed by the limited lattice size and the relation between island size and misfit is subjected to further studies.

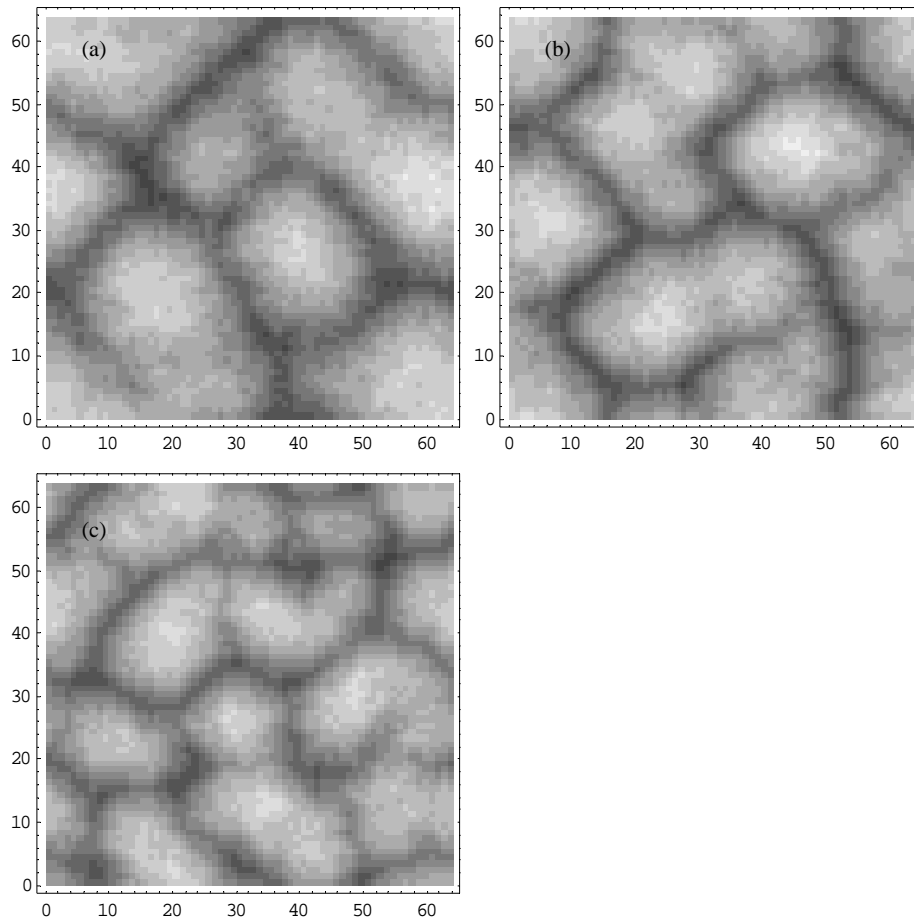


Figure 4.1-5: Snapshots of annealing of film under  $T=1000K$  with misfit  $\epsilon = 6\%$  (a),  $7\%$  (b) and  $8\%$  (c).



## 4.2 Deposition

In the simulations of film growth under deposition, an atom is deposited onto a random surface site after every time period  $\tau$ . For a lattice of area  $L \times L$  in unit of lattice spacings, the time period is given by

$$\tau = \frac{1}{\Phi L^2} \quad (4.2-1)$$

where  $\Phi$  is the deposition rate in unit of mono-layer per second ( $\text{ML s}^{-1}$ ).

Figure 4.2-1 shows the results of deposition under  $T=600\text{K}$ , misfit  $\varepsilon=8\%$  and deposition rate =  $10\text{MLs}^{-1}$ . We observed formation of isolated islands without a wetting layer (Volmer-Weber growth). The deposition rate used is a slow one compared with the intrinsic roughening dynamics. These islands take the shape of a truncated cone, which is an out of equilibrium geometry resulted from the high energy barriers for upper layer formation. Ostward ripening [26] was observed; some small islands shrink and vanish eventually. However, coalescence of islands is suppressed by the elastic repulsion between islands. In fact, the edges of neighboring island are often noticeably deformed to avoid each others.

As in experiments, the deposition rate has a substantial effect on surface morphology. At a lower deposition rate we observed that islands become larger and less dense because there is more time for coarsening. For deposition faster than island formation, layers of atoms quickly accumulate before the resulting film roughens. For a higher deposition rate with an abundant supply of atoms, we observed that the roughening dynamics was similar to that for annealing except for a trivial vertical drift of the whole surface.

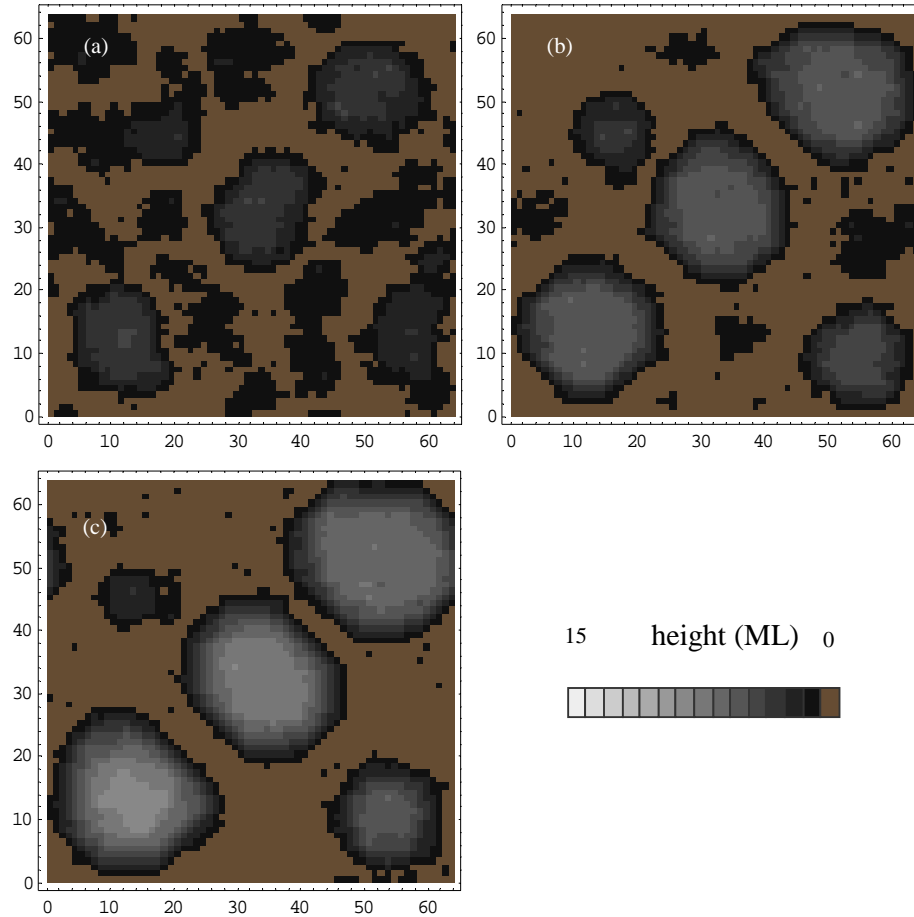


Figure 4.2-1: Surface from simulation of deposition at  $T=600K$  and  $10 \text{ MLs}^{-1}$  with misfit  $\varepsilon=8\%$  at nominal thickness of (a) 0.8ML, (b) 1.4ML and (c) 2ML thick. The substrate is indicated by the brown color in the background.

For deposition at high temperature  $T=1000K$  with the same misfit  $\varepsilon=8\%$  and deposition rate  $=20000 \text{ MLs}^{-1}$ , isolated semi-spherical 3D islands were observed as shown in Figure 4.2-2. At the rate considered above, island growth is limited by the supply of atoms. These individual islands have already relaxed to their equilibrium shapes during the growth process. The smooth and spherical surface of the island we observed suggests that the surface is not a faceted one, and the ATG theory applies. The



morphology dependence on the deposition rate observed at low temperature is also applicable for the high temperature case.

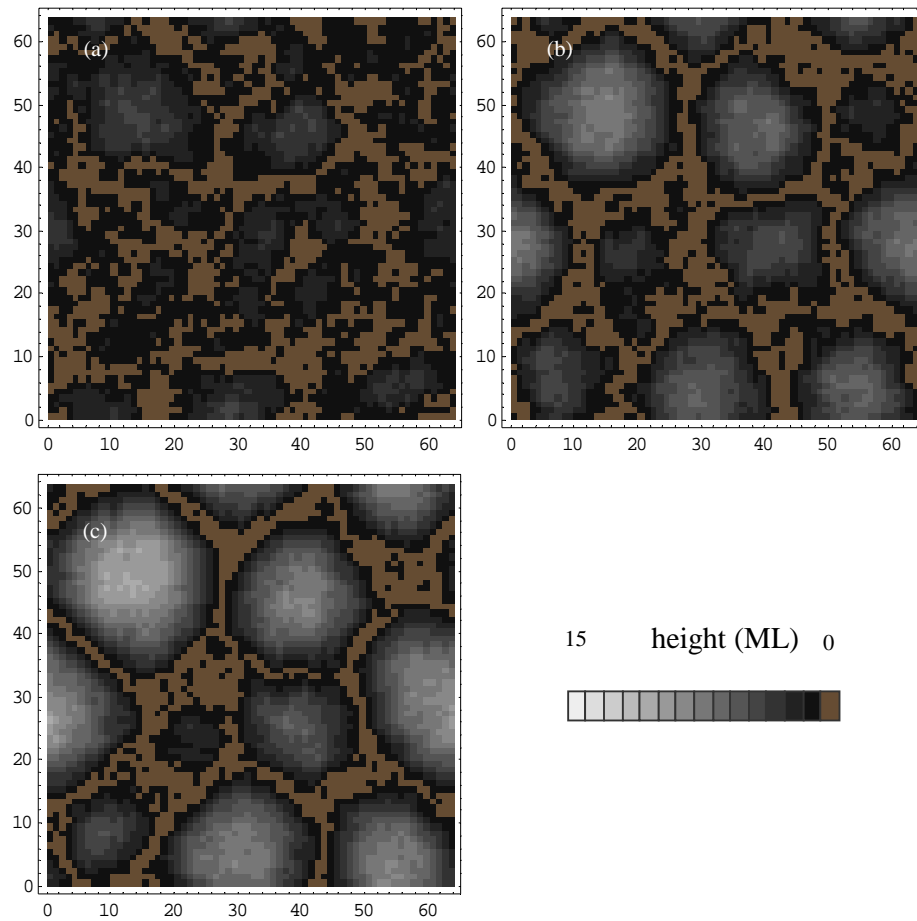


Figure 4.2-2: Surface from simulation of deposition at  $T=1000K$  and  $20000 \text{ MLs}^{-1}$  under misfit  $\mathcal{E}=8\%$ . (a) 1ML, (b) 2ML and (c) 3ML thick.



## 4.3 Pits and grooves

One particular interesting observation is the transition from pits to grooves, which was observed in our annealing simulations. For shallow pits, a square base is energetically preferred to a rectangular one, as shown in Figure 4.3-1 (a) and Figure 4.3-2 (a). As the pits develop, their sidewalls also become steeper due to the increasing importance of the elastic energy term. Grooves are then energetically preferred to rounded pits because of their larger linear extent which can lead to stress relief over much wider regions. Grooves can also be formed by coalescing of a pair of pits as shown in Figure 4.3-1 (b). Their growth is often enhanced by the stress around a 2D island as shown in Figure 4.3-1 (c). However, pits can also turn into grooves independently far away from islands as shown in Figure 4.3-2. We have also carried out simulation on deposition at smaller scales, pits and grooves formation are also observed. Anisotropic pit elongation is observed in an experiment carried out by Gray *et al*, as shown in Fig 1 of [10], which shows groove morphology similar to that in Figure 4.3-1 (c).

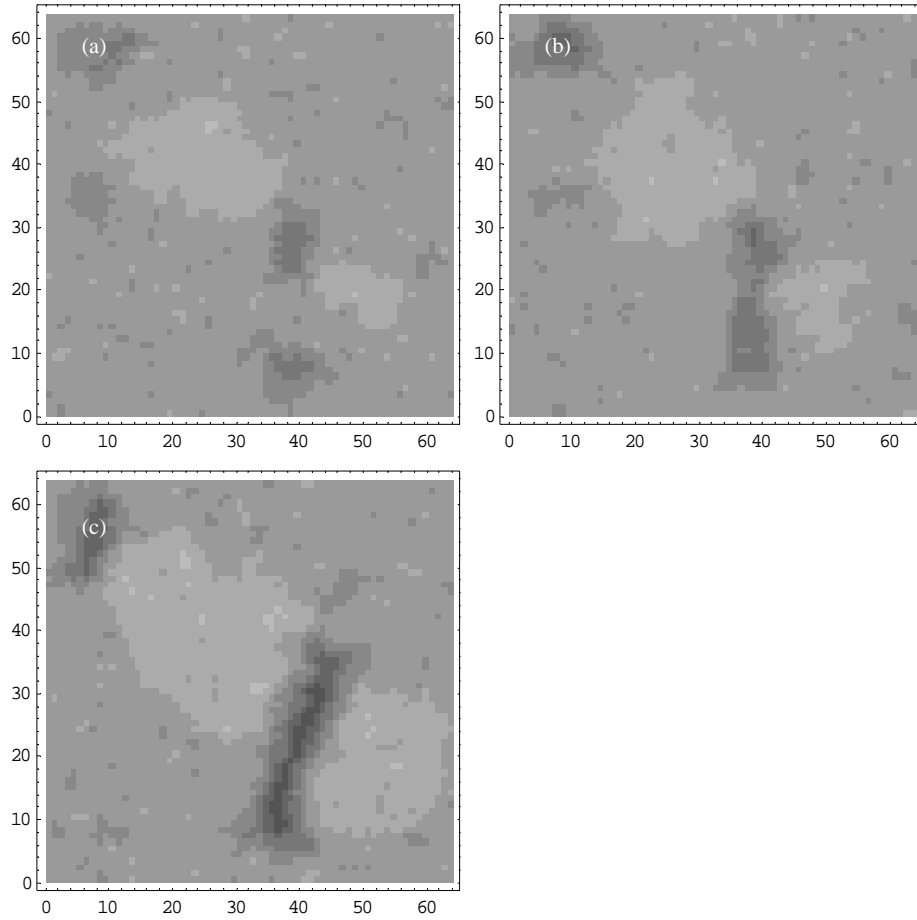


Figure 4.3-1: Groove formation from annealing of film under  $T=600K$  with misfit  $\mathcal{E}=6\%$ .

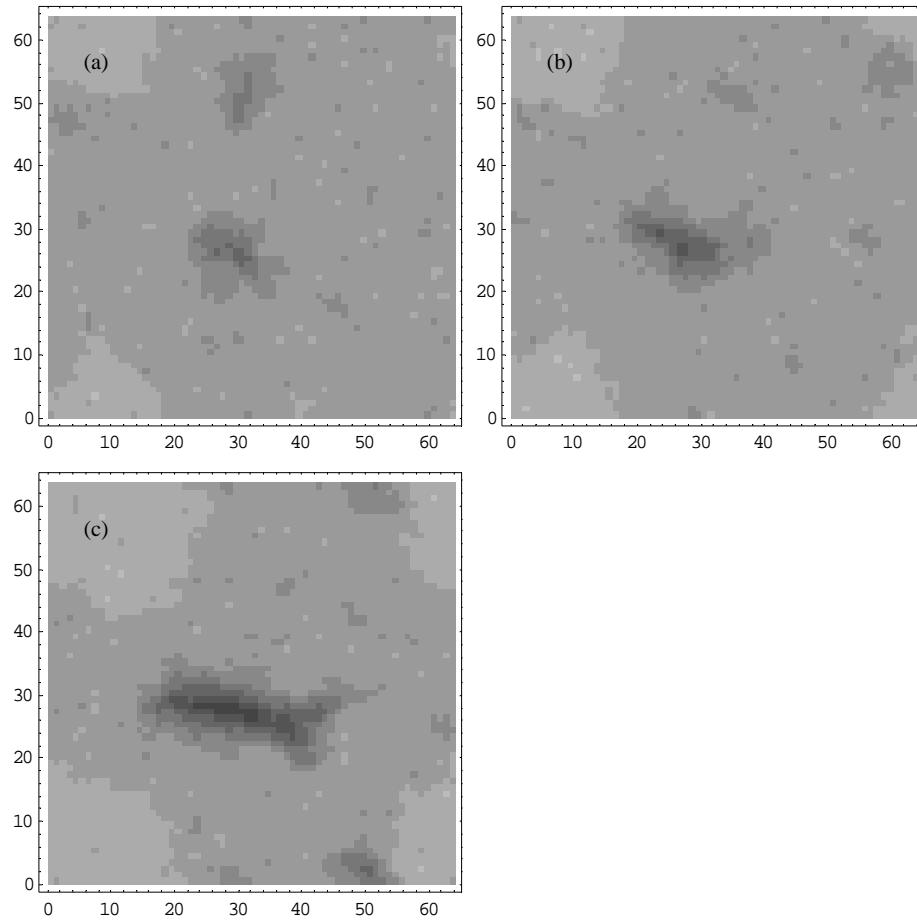


Figure 4.3-2: Snapshots of annealing of film under  $T=600K$  with misfit  $\mathcal{E}=6\%$  showing a pit turning into a groove far away from the influence of any 2D island.



## 5. Conclusions

In conclusion, we have studied the roughening of strained heteroepitaxy in 3D. The accelerated algorithms introduced in chapter 2 greatly improve the computational performance of the simulations. They also account for the long ranged elastic interaction accurately, which is essential for ripple growth. Systems of substrate with dimensions  $64 \times 64 \times 64$  were simulated. Typically  $10^6$  atomic hopping steps are involved and take within 10 days on a 2GHz desktop computer.

With these fast algorithms, we simulated annealing and deposition of strained heteroepitaxial layers. In the simulations of high temperature annealing, we observed ripples and subsequently gradual island formation consistent with the ATG instability theory. For the case of low temperature annealing, islands or pits are formed via the nucleation pathway, and the pits can later turn into grooves. These show that the island formation mechanism depends strongly on temperature. We also suggest that the selection mechanisms between islands and pits as well as between pits and grooves are of energetic origin. For the simulations of deposition, morphologies depend dramatically on whether deposition is slow compared to the intrinsic roughening rate of the surface. For slow deposition, isolated semi-spherical islands are formed because of the limited supply of atoms. In contrast during fast deposition, 3D structures form only after layers of atoms have accumulated and are similar to those from annealing of initially flat films.



## References

- [1] M. Volmer and A. Weber: *Z. Phys. Chem.*, Vol. 119, pp. 277 (1926).
- [2] F. C. Frank and J. H. van der Merwe: *Proc. R. Soc. Londom, Ser. A*, Vol 198, pp. 205 (1949).
- [3] I. N. Stranski and L. Von Krastanov: *Sitz. Ber. Akad. Wiss. Let. Mainz Math.-Natur.*, Vol. 146, pp. 797 (1939).
- [4] Y.-W. Mo, D. E. Savage, B. S. Swartzentruber and M. G. Lagally: “Kinetic Pathway in Stranski-Krastanov Growth of Ge on Si(001)”. *Physical Review letters*, Vol. 65, pp. 1020-1023 (1990).
- [5] M. Tomitori, K. Watanabe, M. Kobayashi and R. M. Tromp: *Surf. Sci.* 349, 129 (1996).
- [6] P. Sutter and M. G. Lagally: “Nucleationless Three-Dimensional Island Formation in Low-Misfit Heteroepitaxy”, *Physical Review Letters*, Vol. 84, pp. 4637-4640 (2000).
- [7] J. A. Floro, E. Chason, L. B. Freund, R. D. Twisten, R.Q. Hwang and G. A. Lucadam: “Evolution of coherent islands in  $\text{Si}_{x-1}\text{Ge}_x/\text{Si}(001)$ ” *Physical Review B*, Vol. 59, pp. 1990-1998 (1999).
- [8] D. Vanderbilt and L. K. Wickham: *Elastic energies of coherent germanium islands on silicon*, *Mater. Res. Soc. Proc.* 202, 555 (1991).
- [9] J. A. Floro, J. L. Gray, N. Singh, D. M. Elzey and R. Hull: “Kinetic Size Selection Mechanisms in Heteroepitaxial Quantum Dot Molecules” *Physical Review Letters*, Vol. 92, pp. 135504 (2004).



- [10] J. L. Gray, R. Hull and J. A. Floro: “Formation of one-dimensional surface grooves from pit instabilities in annealed SiGe/Si(100) epitaxial films” *Applied Physics Letters*, Vol. 85, pp. 3253-3255 (2004).
- [11] M. Volmer and A. Weber: *Z. phys. Chem.* 119, 277 (1925).
- [12] R. J. Asaro and W. A. Tiller: “Interface morphology development during stress corrosion cracking”. *Metallurgical Transactions A*, Vol. 3, pp. 1789 (1972).
- [13] M. A. Grinfeld: “Instability of the separation boundary between a non-hydrostatically stressed elastic body and a melt”. *Soviet Physics Doklady*, Vol 31, pp. 831-834 (1986).
- [14] D. J. Srolovitz: “ON THE STABILITY OF SURFACES OF STRESSED SOLIDS”. *Acta metallurgica*, Vol. 37, pp. 621-625 (1989).
- [15] B. G. Orr, D. Kessler, C. W. Snyder and L. Sander: “A Model for Strain-Induced Roughening and Coherent Island Growth”, *Europhysics Letters*, Vol. 19(1), pp. 33-38 (1992).
- [16] F. Much and M. Biehl, *Euro. Physical Review Letters*, Vol. 63, pp. 14 (2003).
- [17] C.-H. Lam, C.-K. Lee and L. M. Sander: “Competing roughening mechanisms in heteroepitaxy: a fast kinetic Monte Carlo Study”. *Physical Review Letters*, Vol. 89, 216102 (2002).
- [18] A. Pimpinelli and J. Villain: *Physics of crystal growth*, Cambridge University Press (1998).
- [19] M. E. J. Newman and G. T. Barkema: *Monte Carlo Methods in Statistical Physics*, Oxford University Press (1999).



- [20] J. Dongarra, A. Lumsdaine, R. Pozo and K. Remington: “The Iterative Methods Library”. *Proceedings of the Second Object Oriented Numerics Conference*, pp. 214-218 (1992). <http://math.nist.gov/iml++/>
- [21] W. H. Press, S. A. Teukolsky, W. T. Vetterling and B. P. Flannery: “Conjugate Gradient Methods in Multidimensions”. *Numerical Recipes in C*, Cambridge University Press, USA, pp. 420-422 (1992).
- [22] “Math Kernel Library”. <http://www.intel.com/software/products/mkl/>
- [23] “The Cygwin project”. <http://www.cygwin.com/>
- [24] D. E. Jesson, K. M. Chen, S. J. Pennycook, T. Thundat and R. J. Warmack, *Physical Review letters*, Vol. 77, pp. 1330 (1996)
- [25] D. Vanderbilt and L. K. Wickham: “In Evolution of Thin-Film and Surface Microstructure”. C. V. Thompson *et al* Ed., *MRS Symposia Proceedings* No. 202 (MRS, Pittsburgh, 1991), p. 555.
- [26] D. E. Jesson, T. P. Munt, V. A. Shchukin and D. Bimberg: *Physical Review B*, Vol. 69, pp. 041302 (2004).